

國立中央大學

物理學系
學論文
碩士

Search for Heavy Resonances Decaying into a Pair of
Higgs Bosons in the Four b quark Final State from pp
Collisions at $\sqrt{s} = 13$ TeV with the CMS Detector

研究生：陳勁璋
指導教授：余欣珊

中華民國 一〇六年六月



國立中央大學圖書館 碩博士論文電子檔授權書

(104 年 5 月最新修正版)

本授權書授權本人撰寫之碩/博士學位論文全文電子檔(不包含紙本、詳備註 1 說明)，在「國立中央大學圖書館博碩士論文系統」。(以下請擇一勾選)

同意 (立即開放)

同意 (請於西元 _____ 年 _____ 月 _____ 日開放)

不同意，原因是：_____

在國家圖書館「臺灣博碩士論文知識加值系統」

同意 (立即開放)

同意 (請於西元 _____ 年 _____ 月 _____ 日開放)

不同意，原因是：_____

以非專屬、無償授權國立中央大學、台灣聯合大學系統圖書館與國家圖書館，基於推動「資源共享、互惠合作」之理念，於回饋社會與學術研究之目的，得不限地域、時間與次數，以紙本、微縮、光碟及其它各種方法將上列論文收錄、重製、與利用，並得將數位化之上列論文與論文電子檔以上載網路方式，提供讀者基於個人非營利性質之線上檢索、閱覽、下載或列印。

研究生簽名: 陳勁瑋 學號: 105222028

論文名稱: Search for Heavy Resonances Decaying into a Pair of Higgs Bosons in the Four b quark Final State from pp Collisions at $\sqrt{s} = 13$ TeV with the CMS Detector

指導教授姓名: 余欣珊

系所 : 物理 所 博士班 碩士班

填單日期 : 2017/07/17

備註 :

1. 本授權書之授權範圍僅限**電子檔**，紙本論文部分依著作權法第 15 條第 3 款之規定，採推定原則即預設同意圖書館得公開上架閱覽，如您有申請專利或投稿等考量，不同意紙本上架陳列，須另行加填申請書，詳細說明與紙本申請書下載請至本館數位博碩論文網頁。
2. 本授權書請填寫並**親筆**簽名後，裝訂於各紙本論文封面後之次頁（全文電子檔內之授權書簽名，可用電腦打字代替）。
3. 讀者基於個人非營利性質之線上檢索、閱覽、下載或列印上列論文，應遵守著作權法規定。

從質子質子對撞在質量中心能量 13 兆電子伏特利用緊湊渺子偵測器尋找重粒子衰變到一對希格斯粒子於四個底夸克最終態

摘要

論文將呈現尋找重粒子衰變到一對希格斯粒子於四個底夸克最終態。分析基於大強子對撞機在質量中心能量 13 兆電子伏特利用緊湊渺子偵測器在 2016 收集的數據，總亮度為 35.9fb^{-1} 。希格斯粒子是由正反底夸克對重建而成。希格斯噴流將由其質量、 τ_{21} 與底夸克標記選定。95% 信心水準利用 CLs 計算生產截面乘以衰變分支上限介於重粒子的質量從 1.2 兆電子伏特到 3 兆電子伏特低於 10 fb.

Search for Heavy Resonances Decaying into a Pair of Higgs Bosons in the Four b quark Final State from pp Collisions at $\sqrt{s} = 13$ TeV with the CMS Detector

by

Ching-Wei Chen

Submitted to the Department of Physics
on July 18, 2017, in partial fulfillment of the
requirements for the degree of
Master of Physics

Abstract

A search for heavy resonances decaying to a pair of Higgs bosons in the four b quark final state is presented. The analysis is based on the data collected in 2016 with the CMS detector at LHC at center-of-mass energy $\sqrt{s} = 13$ TeV, corresponding to integrated luminosity of 35.9 fb^{-1} . The Higgs bosons are reconstructed from high momentum $b\bar{b}$ quark pairs. The mass variable, τ_{21} discriminator, and double-b tagger are used for Higgs tagging. The signal regions are separated by double-b tagger into two categories. A 95% upper limit on the production cross section of $\sigma_X \times \mathcal{B}(X \rightarrow HH \rightarrow b\bar{b}b\bar{b})$ is obtained from the combination of two categories with a limit below 10 fb for m_X from 1200 to 3000 GeV.

Thesis Supervisor: Shin-Shan Eiko Yu

Title: Associate Professor

Contents

| | | |
|----------|---|-----------|
| 1 | Introduction and Theory Overview | 1 |
| 1.1 | Introduction | 1 |
| 1.2 | Theory | 2 |
| 1.2.1 | Waped Extra Dimension | 2 |
| 1.2.2 | Motivation | 5 |
| 2 | Collider and Detector | 7 |
| 2.1 | Large Hadron Collider | 7 |
| 2.2 | The Compact Muon Solenoid Detector | 7 |
| 2.2.1 | Detector Kinematics | 9 |
| 2.2.2 | Magnet System | 9 |
| 2.2.3 | Tracker Detector | 10 |
| | Pixel Trackers | 11 |
| | Strip Trackers | 11 |
| 2.2.4 | Electromagnetic Calorimeter | 11 |
| 2.2.5 | Hadron Calorimeter | 12 |
| 2.2.6 | Muon Detector | 13 |
| 2.3 | The trigger system | 14 |
| 3 | Analysis Strategy | 15 |
| 3.1 | Data and Simulated Samples | 15 |
| 3.2 | Monte Carlo Simulation | 15 |
| 3.3 | Event Reconstruction and Selection | 17 |
| 3.3.1 | Higgs Jet Reconstruction | 19 |

| | | |
|---------------------|--|-----------|
| 3.3.2 | Heavy Resonance Selection | 21 |
| 3.3.3 | Higgs Tagging Selection | 22 |
| 3.4 | Triggers | 25 |
| 3.5 | Simulation Distribution | 26 |
| 3.6 | Data and Monte Carlo Comparison | 28 |
| 4 | Background Estimation | 37 |
| 4.1 | Bump Hunt | 37 |
| 4.2 | Alphabet | 37 |
| 4.3 | Alphabet Assisted Bump Hunt | 41 |
| 4.3.1 | Signal model | 42 |
| 4.3.2 | Background model | 42 |
| 5 | Systematic Uncertainty | 45 |
| 5.1 | Systematic Uncertainty on Signal Selection | 45 |
| 5.2 | Summary table | 51 |
| 6 | Final Result | 53 |
| 6.1 | Asymptotic CLs | 53 |
| 6.2 | 95% upper limit | 55 |
| 6.3 | Conclusion | 56 |
| Bibliography | | 57 |
| A | Optimization of the Selection | 63 |
| A.1 | $\Delta\eta$ | 63 |
| A.2 | Double-b Tagger | 66 |
| A.3 | Mass of AK8 Jet | 68 |

List of Figures

| | | |
|-----|--|----|
| 1.1 | The feynman diagram of $q\bar{q} \rightarrow X \rightarrow HH \rightarrow b\bar{b}b\bar{b}$ | 2 |
| 2.1 | The three-dimension sketch-up image of the CMS detector[28]. | 8 |
| 3.1 | The comparison of M_{jj} and reduced mass distribution of bulk graviton $M_X = 1.4$ (left) and 2.5 TeV (right). The mean and the σ/mean of a Gaussian fit to the distribution are shown. | 22 |
| 3.2 | The cut flow of all M_X (GeV) of spin-0 radion (left) and of spin-2 bulk graviton (right). | 28 |
| 3.3 | The comparison of signal and background. The signals of $M_X = 1.4$ TeV and 2.5 TeV from both models are shown. The cross section is set to 20 pb in the figures. Multi-jet events are seperated into four categories summarized in the table 3.10. From top to bottom are the comparison of p_T , η , and double-b tagger of leading (left) and next leading (right) AK8 jet. | 29 |
| 3.4 | The comparison of signal and background. The signals of $M_X = 1.4$ TeV and 2.5 TeV from both models are shown. The cross section is set to 20 pb in the figures. Multi-jet events are seperated into four categories summarized in the table 3.10. From top to bottom are the comparison of PUPPI soft-drop mass, τ_{21} of leading (left) and next leading (right) AK8 jet, the reduced mass (bottom left), and $ \Delta\eta$ (the two leading AK8 jets) (bottom right). . . | 30 |

| | |
|---|----|
| 3.5 The comparison of data and background of pile-up distribution with (left) and without (right) pile-up re-weighting. Multi-jet events are seperated into four categories summarized in the table 3.10. | 31 |
| 3.6 The comparison of data and background in inverse double-b region. Multi-jet events are seperated into four categories summarized in the table 3.10. From top to button are the comparison of p_T , η , and double-b tagger of leading (left) and next leading (right) AK8 jet. | 32 |
| 3.7 The comparison of data and background in inverse double-b region. Multi-jet events are seperated into four categories summarized in the table 3.10. From top to button are the comparison of PUPPI soft-drop mass, τ_{21} of leading (left) and next leading (right) AK8 jet, the reduced mass (button left), and $ \Delta\eta $ (the two leading AK8 jets) (button right). | 33 |
| 3.8 The comparison of data and background in inverse τ_{21} region. Multi-jet events are seperated into four categories summarized in the table 3.10. From top to button are the comparison of p_T , η , and double-b tagger of leading (left) and next leading (right) AK8 jet. | 34 |
| 3.9 The comparison of data and background in inverse τ_{21} region. Multi-jet events are seperated into four categories summarized in the table 3.10. From top to button are the comparison of PUPPI soft-drop mass, τ_{21} of leading (left) and next leading (right) AK8 jet, the reduced mass (button left), and $ \Delta\eta $ (the two leading AK8 jets) (button right). | 35 |
| 4.1 The cartoon of a bump on the background. | 38 |
| 4.2 The cartoon of a two dimensional distribution. | 39 |

| | | |
|-----|---|----|
| 4.3 | The double-d tagger versus the mass of the leading AK8 jet distribution in TT (left) and LL (right) region. | 39 |
| 4.4 | The $R_{p/f}$ and its quadratic fit in TT (left) and LL (right) region. | 40 |
| 4.5 | The predicted background from data in TT (left) and LL (right) region. | 40 |
| 4.6 | The p.d.f. of signal model in TT (left) and LL (right) category. The signal of Bulk raviton is used. The p.d.f.s are normalized to integral of all probability of one. | 42 |
| 4.7 | The pre-fit and post-fit on the data in anti-tag region (left) and signal region (right) in LL category (top) and TT category (bottom). | 43 |
| 5.1 | The pile-up uncertainty. The scale-up and scale-down to central ratio based on the change of the upper limit are shown in TT (left) and LL (right) category. | 46 |
| 5.2 | The double-b tagger uncertainty. The scale-up and scale-down to central ratio based on the change of the upper limit are shown in TT (left) and LL (right) category. | 47 |
| 5.3 | The jet energy resolution uncertainty. The scale-up and scale-down to central ratio based on the change of the upper limit are shown in TT (left) and LL (right) category. | 48 |
| 5.4 | The jet energy scale uncertainty. The scale-up and scale-down to central ratio based on the change of the upper limit are shown in TT (left) and LL (right) category. | 49 |
| 5.5 | The Factorization uncertainty. The scale-up and scale-down to central ratio based on the change of the efficiency are shown in TT (left) and LL (right) category. | 49 |
| 5.6 | The jet energy scale uncertainty. The values of ratio RMS of efficiency from 100 p.d.f. sets to efficiency of central value are shown in TT (left) and LL (right) category. | 50 |

| | | |
|-----|---|----|
| 6.1 | The 95% upper limit on signal cross section \times branch ratio ($pp \rightarrow X \rightarrow HH \rightarrow b\bar{b}b\bar{b}$) of bulk graviton (left) and radion (right). | 55 |
| A.1 | The distribution of $\Delta\eta$ of 1.4 TeV bulk graviton and of multi-jet in TT (left) and LL (right) category. | 64 |
| A.2 | The Punzi significance of different cut value of $\Delta\eta$ in TT (left) and LL (right) category of bulk graviton. | 64 |
| A.3 | The Punzi significance of different cut value of $\Delta\eta$ in TT (left) and LL (right) category of radion. | 65 |
| A.4 | The 95% upper limit on $\sigma(pp \rightarrow X \rightarrow HH) \times Br(HH \rightarrow b\bar{b}b\bar{b})$ with different double-b tagger category. | 67 |
| A.5 | The weights versus jet p_T of W boson and of Higgs boson correction. | 69 |
| A.6 | The corrected PUPPI soft-drop mass (left) filled with leading and next leading AK8 jets and the mean of the Gaussian fit on the mass of versus the jet p_T (right). One point on the curve corresponds to one mass point of signal. | 69 |
| A.7 | The 95% upper limit on $\sigma(pp \rightarrow X \rightarrow HH) \times Br(HH \rightarrow b\bar{b}b\bar{b})$ with different mass windows of different mass correction. | 69 |

List of Tables

| | | |
|------|--|----|
| 3.1 | List of datasets used in the analysis and its corresponding integrated luminosity in pp collision at $\sqrt{s} = 13$ TeV. | 16 |
| 3.2 | List of bulk graviton $\rightarrow HH \rightarrow b\bar{b}$ Monte Carlo simulation and its corresponding cross section and the number of events. The cross sections are used in McM process at leading order, LO, and not used in the final results. | 16 |
| 3.3 | List of radion $\rightarrow HH \rightarrow b\bar{b}$ Monte Carlo simulation and its corresponding cross section and the number of events. The cross sections are used in McM process at LO and not used in the final results. | 17 |
| 3.4 | List of multijet Monte Carlo simulation and its corresponding cross section and the number of events. The cross sections are used in McM process at LO. | 17 |
| 3.5 | List of the cross section \times the branch ration of HH decay in fb. The model $k/\bar{M}_{Pl} = 0.1$ in bulk graviton is considered, and the model $\Lambda_R = 3$ TeV and $kl = 35$ of radion is considered. | 18 |
| 3.6 | List of MET filters applied in the analysis. | 18 |
| 3.7 | List of the tight PF jet identification. | 21 |
| 3.8 | List of Triggers applied in the analysis. | 25 |
| 3.9 | List of all selection in the analysis. | 26 |
| 3.10 | The cut flow of all M_X (GeV) of spin-0 radion. | 26 |
| 3.11 | The cut flow of all M_X (GeV) of spin-2 bulk graviton. | 27 |
| 3.12 | List of categorization of multijet events. | 27 |

| | | |
|-----|---|----|
| 5.1 | List of systematic uncertainties and their values. | 51 |
| 6.1 | The table of 95% upper limit on signal cross section \times branch ratio ($pp \rightarrow X \rightarrow HH \rightarrow b\bar{b}b\bar{b}$). | 55 |
| A.1 | The mass windows used for optimization. | 68 |

Chapter 1

Introduction and Theory Overview

1.1 Introduction

The analysis is aim at searching for heavy resonances decaying to a pair of Higgs bosons in the four b quark final state using 35.9 fb^{-1} proton-proton collision data at center-of-mass energy 13 TeV collected with the CMS detector at the LHC. The figure 1.1 shows the feynman diagram of the channel.

The Higgs tagging process uses the b-tagging algorithm, N-subjetness variable, and the mass of the jets. The analysis is searching for a bump in the dominant background of multi-jet events.

In [chapter 1](#), an overview of Wrapped Extra Dimension theory, signal model, and motivation is presented. In [chapter 2](#), the LHC and the CMS detector are simply introduced. In [chapter 3](#), the information of the data and the Monte Carlo Simulation is shown along with the comparison of shape of each discripant variable. The reconstruction and the selection of the event is also fully detailed. In [chapter 4](#), the background estimation method based on data driven is presented. All sysyematic uncertainted considered is documented in [chapter 5](#). Finally, the result of 95% CL_s upper limit of cross section \times branch ratio is shwon in [chapter 6](#).

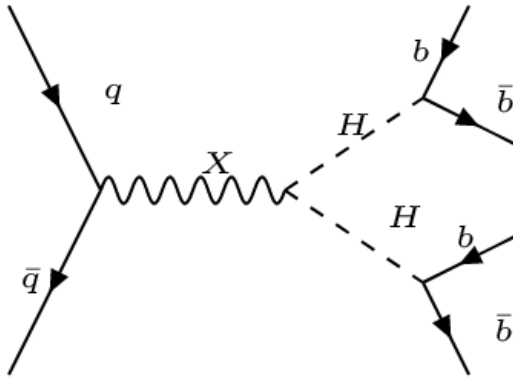


FIGURE 1.1: The feynman diagram of $q\bar{q} \rightarrow X \rightarrow HH \rightarrow b\bar{b}b\bar{b}$.

1.2 Theory

The discovery of the boson whose mass around 125 GeV and with properties close to Higgs mechanism in the standard model (SM) has incited the search under Higgs potential including Higgs self-coupling[1, 2]. Especially, it is a channel worth exploring and finding new physic beyond the SM. Targeting heavy resonance, the model Wrapped Extra Dimension is considered.

1.2.1 Wraped Extra Dimension

To solve the hierarchy problem, Wrapped Extra dimension proposed by Randall and Sundrum postulates a scenario that the SM particles and forces associating with gravity force are confined to a four-dimension subspace within (4+n)-dimension spacetime, referred to as "3-brane", to explain the fact that we do not see experimental signs of the extra dimensions[3]. The spacetime metrix takes the form[4]:

$$ds^2 = e^{-2\sigma(\phi)} \eta_{\mu\nu} dx^\mu dx^\nu + r_c^2 d\phi^2, \quad (1.1)$$

where μ and ν run over 1, 2, 3, and 4, and ϕ is the fifth dimension. Its classical action is

$$S = S_{Gravity} + S_{TeV} + S_{Planck} + S_{Matter}, \quad (1.2)$$

, where $S_{Gravity}$ is the action of bulk gravity, and S_{Matter} is the action of matter field. The actions can be written as:

$$\begin{aligned} S_{i=TeV/Planck} &= - \int d^4x \sqrt{g(\phi = 0, \pi)} \Lambda_{i=TeV/Planck} \\ S_{Gravity} &= \int d^4x \int_{\pi}^{\pi} d\phi \sqrt{g} (-\Lambda_{bulk} + 2M_5^3 R), \end{aligned} \quad (1.3)$$

where Λ is hte vacuum energy density, R is Ricci metrix. We arrive at:

$$\begin{aligned} \sigma(\phi) &= r_c |\phi| \sqrt{\frac{-\Lambda}{24M_5^2}} \equiv r_c |\phi| k \\ k &\equiv \sqrt{\frac{-\Lambda}{24M_5^2}}, \end{aligned} \quad (1.4)$$

where k is referred as curvature factor. We can integrate the fifth dimension and get four-dimension Planck mass:

$$\bar{M}_{Pl}^2 = \frac{M_5^3}{k} (1 = e^{-2\pi k r_c}). \quad (1.5)$$

Finally, we get the spacetime metrix:

$$ds^2 = e^{-2kr_c\phi} \eta_{\mu\nu} dx^\mu dx^\nu + r_c^2 d\phi^2, \quad (1.6)$$

where k is a scale of the order of the Planck scale, x^μ are coordinates for the familiar four dimensions, while $0 \leq \phi \leq \pi$ is the coordinate for an extra

dimension, which is a finite interval whose size is set by r_c . The exponential is the source of large hierarchy between weak and the observed Planck scale.

There are models predicting the existence of new particles, such as spin-0 radion and spin-2 graviton[5–7]. For example, a radion scalar is added to stabilize the r_c in RS theory without a fine-tuning of parameters[8]. Other model proves that a radion field can remove the constraints between two branes without a stabilized radius[9], and that a radion scalar can exist with radius stabilization in bulk scalar field while assuming stabilization exists[10]. A possible mixing of the radion which is the only graviscalar in RS model and the Higgs is proposed[11]. However, according to the latest experimental data, the mixing is expected to be small. Therefore, the contribution of the mixing is not considered in this analysis[12].

We follow the ref.[13] to calculate the cross section of bulk graviton.

$$gg \rightarrow KK\text{graviton} \rightarrow ZZ, WW, hh(\text{and } t\bar{t}, b\bar{b}) \quad (1.7)$$

$$L_{\text{prod.}} = 0.053 \left(\frac{k}{M_{Pl} M_G} \right) \eta^{\mu\alpha} \eta^{\nu\beta} h_{\alpha\beta}^{(1)} T_{\mu\nu}^{\text{gluon}}(x),$$

where the M_G is the mass of KK graviton, and $T_{\mu\nu}^{\text{gluon}}$ is four-dimesion four-momentum of SM gluon. The implementation of the calcuation is described in ref.[4]. The model which is capable of calculating the correction of next-to-leading-order QCD induced spin-2 particle is used. The cross section is calculated by MG5_aMC@NLO. Because of the Higgs-like property of radion, the cross section of radion is calculated by rescaling the cross section of Higgs like particle[13, 14]. The production of Higgs-like particle by gluon-gluon fusion is followed by ref.[15, 16], which is calcuated in next-to-next-to-leading-order QCD induced soft-gluon resummation. The Higgs-like calculation is up to 1 TeV, and it is constant for mass above 1 TeV. The cross section of radion is based on the cross section of Higgs-like multiplied by k factor. In the calcuation of both signal, CTEQ6LPDF is used[17].

1.2.2 Motivation

There are models predicting heavy resonances decaying into VV[18]. Several researches on these channels are performed in both CMS and ATLAS. There are also the combinations of these analyses[19–22]. The combination from ATLAS excludes the resonance of Bulk Graviton from below 810 GeV at $\sqrt{s} = 8$ TeV[23], and despite the combination from CMS fails to exclude any mass spectrum of Bulk Graviton given a less sensitive model, it sets the upper limit of 700 to 10 fb of cross section of Bulk Graviton through M_X from 600 to 2500 GeV at $\sqrt{s} = 8$ TeV[24]. Searches for Bulk Graviton decaying into HH in four b-flavored quarks final state have been performed by CMS and ATLAS at $\sqrt{s} = 8$ TeV[25, 26]. They exclude the mass region below 830 and 720 GeV respectively. The intermediate region of the mass of heavy resonances ($M_X \approx 2$ TeV) is left interesting to be explored.

Chapter 2

Collider and Detector

2.1 Large Hadron Collider

Large Hadron Collider locates at Geneva region about 100 meters underground which is built and operated by European Organization for Nuclear Research, CERN. Its circumference is 27-km-long, and its two proton beams in which the energy of each proton is 6.5 TeV produce collisions at center-of-mass energy reaching 13 TeV in 2015. It is currently both the largest in size and highest center-of-mass energy collider in the world. Besides, LHC also provides heavy-ion collision to include the study of the behavior of quantum chromo dynamics, QCD, under high density parton mementum fraction. When it operates, the intervals between proton bunch crossing is 25 ns, that is to say, 4×10^7 events are produced per second. Besides, an average of 20 unelastic collision will be produced in a signle bunch crossing. It is undoubtly challenging requirement on techique not only to reduce the number of events recorded by triggers but also to alleviate the effect by vertices of unelastic collision from pile-ups.

2.2 The Compact Muon Solenoid Detector

As one of the detectors of the LHC, the Compact Muon Solenoid Detector, CMS[27], shares the same aims of the LHC. Basically, it will elucidate the physical properties of the Higgs boson whose mass is around 125 GeV, and it will also test the

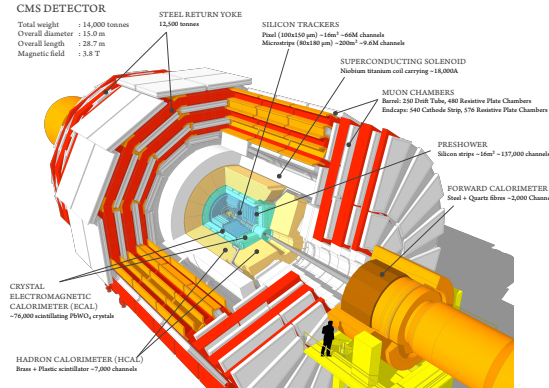


FIGURE 2.1: The three-dimension sketch-up image of the CMS detector[28].

mathimatical consistency of Standard Model, SM, at TeV scale. People also hope to find the new physic beyond SM where Supersymmetry and Extra Dimension is often being considered. The latter nessisates the finding of the Graviton in TeV scale. All researches need a delicate disign of a detector, including good charged particle reconstruction to trace the vertex, good EM energy resolution, and good measurement on missing transverse momentum and di-jet reslotion.

- The tracker: The high granularity tracker at inner detector can well reconstruct the trace of charged particles. It is also indispensable for indentifying b-flavored jets and τ .
- The muon chamber: The muon chamber combined with tracker information under the magnetic field of opposite direction can together interpolate to reduce mis-matching rate in muon reconstruction and identify the cosmic muons from outside of the detector.
- The calorimeters: The calorimeters facilitate the shower and measure the energy of post-shower particles. The information will further be clustered into the energy coresponding to their mother particles.

2.2.1 Detector Kinematics

To better describe the geometry of the detector, a set of axes is set. The z axis is along the beam line, and the positive direction points to counter-clockwise direction of the beam pipe. The x axis points to the center of the circle made up of the beam pipe. The xy plane is perpendicular to z axis and can be described by ϕ :

$$x = r\cos\phi, y = r\sin\phi, \quad (2.1)$$

where ϕ is the azimuthal angle, r is the distance from the z axis on xy plane. The variable rapidity y is related to the angle θ between one vector and the z axis. The difference of rapidity is invariant under boosts along the longitudinal axis. When particles travel near the speed of light, its mass is negligible. Hence, $E \approx |\vec{p}|$ and $\eta \approx y$, while $E = |\vec{p}|$ for a massless particle.

$$y = \frac{1}{2}\ln\left(\frac{E + p_z}{E - p_z}\right), \eta = \frac{1}{2}\ln\left(\frac{|\vec{p}| + p_z}{|\vec{p}| - p_z}\right) = -\log[\tan(\theta/2)] \quad (2.2)$$

2.2.2 Magnet System

In order to have a resolution for charged particles in the trackers, magnetic field must maintain to bend the tracks of charged particles. Providing the magnetic field of CMS, the superconducting solenoid is installed between the calorimeters and muon chambers with diameter of 6.3 m, length of 12.5 m, and mass of 200 t. Designed to have 3.8 T magnetic field at the center of the detector along positive z direction, the solenoid uses four layers based on the Ampere-turn (41.7MA-turn) and made of aluminum alloy. The width of one layer is far less than its counterpart of other detectors, and its lower limit is restricted by the magnetic pressure and the material property of aluminum. It also breaks the convention, for that the magnetic stress is shared between itself and the outer mandrels.

The yoke whose proposes are guiding the magnetic field and absorbing particles except muons and neutrinos is composed of five barrel wheels and 6 end-cap disks[29]. Besides, to avoid the "quench back" effect, where the ebb currents induced in outer mandrels heat up the coil above superconducting critical temperature, a proctecting circuit is designed and worked by either fast discharge or slow discharge through dumping.

2.2.3 Tracker Detector

Having precise reconstructed parimary and secondary vertices, the Tracker detector is designed to be at innerest part of the CMS detector. It needs to be fast enough to collect data between 25 ns interval of bunch crossing and high granularity enough to identify the trajectories. Two kinds of tracker detector are used for difference purpose, the pixel trackers and the strip trackers. While the former is better at determining three dimensional space and at enduring the radiation dose, the latter covers larger total erea since it costs less per area. There are three cylindrical pixel detectors at radii of 4.4, 7.3 and 10.2 cm and two disks of pixel detectors at $|z|$ of 34.5 and 46.5 cm on each side of the interaction point. They together give coverage to pseudorapidity $|\eta| < 2.5$ and an area of about 1 m^2 with total 66 million pixels whose size is $100 \times 150 \mu\text{m}^2$. The strip detectors are seperated into several subsystems. The Tracker Inner Barrel and the Tracker Inner Disk (TIB/TID) at radii extending to 55 cm together, composing 4 layers and 3 disk on each side, provide four $r - \phi$ measurements with resolution $23 \mu\text{m}$ and $35 \mu\text{m}$ by the first two layers and the others respectively. Tracker Outer Barrel (TOB) ranges toward radius of 116 cm and performs six $r - \phi$ measurements with resolution $53 \mu\text{m}$ and $35 \mu\text{m}$ by the first four layers and the others respectively. In addition, Tarcker EndCap (TEC) gives another 9 measurements on ϕ by its nine layers installed at $124 \text{ cm} < |z| < 282 \text{ cm}$.

Pixel Trackers

The pixel trackers are constituted by pn-junctions operated in depletion. When particles pass depletion zone, induced electron-hole pairs will produce signal current and further be amplified and read out. To take the high density radiation dose into account, a n+-doped electrodes in n-doped substratrate design is chosen as sensor. Another advantage of the n-on-n concept is that a guard ring can be made around the sensor to prevent voltage break-down in air ($1.2V/\mu m$). The isolation between electrode prevents electrodes from shortening after radiation. Open p-stop and moderate p-spray are isolation designs implemented on disks and barrel respectively[30].

Strip Trackers

The elements in the trackers are single-side p-on-n silicon micro-strip sensors. Besides, the six inches wafers are used instead of four inches wafers to reduce the cost. As the bulit-on surface charge of $\langle 100 \rangle$ crystal orientation of n substratrate is smaller than $\langle 111 \rangle$ one, the $\langle 100 \rangle$ is chosed to maintain the capacitance after irradiation. The $\langle xyz \rangle$ is the sign used in solid physic, which represents the direction of the plane of a crystal. To clarify, $\langle 100 \rangle$ means the first plane intercepting the x, y, and z axis at 1, 0, and 0 respectively. Other planes are perpendicular to this plane and have distance by $\sqrt{1^2 + 0^2 + 0^2} \times n$. Following the same rule, the first plane in $\langle 111 \rangle$ crystal intercepts the x, y, and z axis at 1, 1, and 1 respectively. Other planes are perpendicular to this plane and have distance by $\sqrt{1^2 + 1^2 + 1^2} \times n$.

2.2.4 Electromagnetic Calorimeter

The electromagnetic calorimeters, ECAL, is used to measure the energy of electromagnetic, EM, particles through EM shower. In the other hand, they can reconstruct the mother particles of electrons and photons indirectly. The system

is composed of the ECAL Barrel (EB) in $|\eta| < 1.479$ and the ECAL Endcap (EE) in $1.479 < |\eta| < 3.0$. Lead-tungstate crystals (PbWO₄) are chosen as scintillator where shower happens. Its short Radiation length (0.89cm) and Moliere radius (2.2cm) is appropriate for compact space in CMS. The photon detectors are set on the back on each crystal. Avalanche photodiodes are used for EB, while vacuum phototriodes are used for EE. Besides, the preshower detector (ES) is installed in front of the EE where $1.653 < |\eta| < 2.6$. There are two layers: lead radiators and silicon strip sensor. The ES is mainly used to identify π^0 and assists the identification of electrons against minimum ionizing particles.

2.2.5 Hadron Calorimeter

The hadron calorimeters measure the energy of hadrons, and they are substantial to detect the neutrinos or exotic particles by measuring missing transverse momentum. There are four subsystems including the barrel (HB) , the endcap (HE) , the outer (HO) , and the forward (HF) designs. Both the HB and the HE are sampling calorimeters. The HB covers $|\eta| < 1.3$, while the HE covers $1.3 < |\eta| < 3$. They are both consisted of scintillators interleaved between C26000 cartridge brass (70% copper and 30% zinc) absorbers because of high density of brass. Six brass layers of 50.5 mm each, eight brass layers of 56.5 mm each along with front and back plate of 40 and 75 mm giving totally 87cm thickness of absorbers in barrel, while the thickness of absorbers in endcap is 79mm for each layer. The HB is not thick enough to contain all the energy of high energy particles. Thus, the HO is installed outside the HB to catch the rest of the later showers combined with the HB to give about 11.8 interaction lengths in total. At the outside of vacuum solenoid, five iron rings each with 2.536m along z axis together form the return yoke. The first layer of each iron ring has one HO layer installed at the outer side, while two layers are installed on inner and outer

sides of the central ring because of its shorest radical distance. Each module includes 10 mm scintillator whose material is Bicron BC408. In addition, to detect the very foward jets thus to improve the measurements of missing transverse momentum, the HF is needed whose coverage extends to about $|\eta| = 5$. As the energy deposit is not uniformly distributed in the detector, the forward region takes higher radiation dose. The HF must be most radiontion-hard by means of the shielding including 40 cm steel, 40 cm concrete, and 5cm of polyethylene. With the same reason, the quartz fibres (fused-silica core and polymer hard-cladding) iis chosen as the absorber material.

2.2.6 Muon Detector

Muon idenification ensures the rate of the expected background is well measured. For example, backgrounds whose final state includes at least one Z boson decaying into di-muons. This is essential for the discovery of Higgs mechianism where backgound of ZZ is domiant. Besides, some physics beyond Standard Model, SuperSuymmetry for example, has muon in its final state. The CMS muon system is made up of three kinds of gaseous chamber detectors. First, the barrel drift tube (DT) chambers contain four layers distributing between $|\eta| < 1.2$. The first three layers include totally 12 chambers, eight for $r - \phi$ measurements and four for $|z|$ measurements, while the last layer only measures $r - \phi$. With a width of single cell of 42 mm, the maximum drift distance is its half, which has 380 ns maximum drift time. The cells filled with 85% Ar and 15% CO₂ set up an electrical field by 3600V anode wire at the central, 1800V two electrode strips at the ceil and the floor, and two 1800V cathode strips on each side. Second, the cathode strip chambers (CSC) have 6 layers and are grouped in 4 stations. Their fast response is suitable for more non-uniform magnetic field and more muons passing through in forward region, so they are placed at $0.9 < |\eta| < 2.4$. The CSC disks are separated into strips by either 20° or 10° in ϕ .

Each chamber has 6 gas gaps with anode wires separated by 7 cathode panels. The cylindrical wires make the r -coordinate measurements, while the charges induced on the strips interpolate to determine ϕ coordinate. The gas mixture is 40% Ar + 50% CO₂ +10% CF₂. Last, the resistive plate chambers (RPC) with fast response are added to muon system to complement the time resolution, especially with multiple-muon events. However, they have to work with DT and CSC, for RPC has less spatial resolution than the others do. There are two layers in each station for the first two stations of DT and one layer in each station for the other two stations. In addition, three disks in the first three CSC to improve the time resolution are used in determination of time of bunch crossing and muon p_T reconstruction. A module consists of 2 gaps in which there is a gas plate held by two bakelites, referred as the up gap and the down gap with a strip between them connecting to the read-out. The triggers in muon system using RPC information can perform at high rate and a rather high p_T of muons threshold.

2.3 The trigger system

The interval between bunch crossing in LHC is 25 ns which corresponds to a rate of events of 40 MHz. The trigger system is required to reduce the rate of events for recording on tape. The system includes Level-1 Trigger system (L1) and High-Level Trigger (HLT) together. The L1 Trigger will reduce at least to 100 kHz, and the HLT will then reduce to a maximum of 30kHz. The L1 Trigger is made up of several hardware programmable electronics which collect information from muon system and calorimeters. On the other hand, the HLT triggers are software-like triggers which have the access to complete readout of data. Thus, they are able to do the complex calculation similar to those done in the analysis off-line. The algorithm of HLT will be improved through the time, so it will not be detailed here.

Chapter 3

Analysis Strategy

The target of the analysis is to search for the heavy resonances decaying to di-Higgs where mass of heavy resonances is above 800 GeV. Each Higgs boson is assumed to further decay to $b\bar{b}$ and is reconstructed in a boosted jet including two b-flavored-like sub-jets by anti-kT08 algorithm. Higgs identification is done by selection on PUPPI soft-drop mass, N-subjetness, and double b-tagger.

3.1 Data and Simulated Samples

The analysis is preformed based on the data collected in pp collision with the CMS detector at $\sqrt{s} = 13$ TeV. The integrated luminosity is 35.9fb^{-1} . Runs in which the detector normally operates was chosen according to the golden JSON file: *Cert_271036 – 284044_13TeV_23Sep2016ReReco_Collisions16_JSON.txt*. The samples of data are listed in table 3.1.

3.2 Monte Carlo Simulation

The Monte Carlo, MC, simulations in the analysis are bulk graviton, radion, and multijet events. MadGraph is used to produce the simulated particles and their decay[31]. Bulk graviton, radion are used for setting the upper limit of cross section, while multijets events are used for testing the background estimation method and not used for final results. The names and the number of events of

| Dataset | Processing | Int. lumi. (fb^{-1}) |
|----------------|------------|--------------------------|
| JetHT/Run2016B | 03Feb2017 | 5.9 |
| JetHT/Run2016C | 03Feb2017 | 2.6 |
| JetHT/Run2016D | 03Feb2017 | 4.4 |
| JetHT/Run2016E | 03Feb2017 | 4.1 |
| JetHT/Run2016F | 03Feb2017 | 3.2 |
| JetHT/Run2016G | 03Feb2017 | 7.7 |
| JetHT/Run2016H | 03Feb2017 | 8.9 |
| Total | | 35.9 |

TABLE 3.1: List of datasets used in the analysis and its corresponding integrated luminosity in pp collision at $\sqrt{s} = 13$ TeV.

samples are listed in the table 3.2-3.4. The cross section of signal used in the final results are listed in the table 3.5[32–35]. Since the distributions of pile-ups of data and of MC are different, a pile-up re-weighting is applied to MC samples. Here the distribution of pile-ups of data is derived by using minibias cross section of pp collision of 69.2 mb[36].

| Samples | $\sigma(pb)$ | Events |
|---|--------------|--------|
| BulkGravTohhTohhbb_narrow_M-1000_13TeV-madgraph | 2.66 | 50000 |
| BulkGravTohhTohhbb_narrow_M-1200_13TeV-madgraph | 0.95 | 50000 |
| BulkGravTohhTohhbb_narrow_M-1400_13TeV-madgraph | 0.37 | 50000 |
| BulkGravTohhTohhbb_narrow_M-1600_13TeV-madgraph | 0.18 | 50000 |
| BulkGravTohhTohhbb_narrow_M-1800_13TeV-madgraph | 0.084 | 48400 |
| BulkGravTohhTohhbb_narrow_M-2000_13TeV-madgraph | 0.041 | 50000 |
| BulkGravTohhTohhbb_narrow_M-2500_13TeV-madgraph | 0.007 | 50000 |
| BulkGravTohhTohhbb_narrow_M-3000_13TeV-madgraph | 0.0017 | 50000 |

TABLE 3.2: List of bulk graviton $\rightarrow HH \rightarrow b\bar{b}$ Monte Carlo simulation and its corresponding cross section and the number of events. The cross sections are used in McM process at leading order, LO, and not used in the final results.

| Samples | $\sigma(\text{pb})$ | Events |
|---|---------------------|--------|
| RadionTohhTohbbhbb_narrow_M-1000_13TeV-madgraph | 1318 | 50000 |
| RadionTohhTohbbhbb_narrow_M-1200_13TeV-madgraph | 116.2 | 50000 |
| RadionTohhTohbbhbb_narrow_M-1400_13TeV-madgraph | 67.97 | 50000 |
| RadionTohhTohbbhbb_narrow_M-1600_13TeV-madgraph | 41.74 | 50000 |
| RadionTohhTohbbhbb_narrow_M-1800_13TeV-madgraph | 26.57 | 50000 |
| RadionTohhTohbbhbb_narrow_M-2000_13TeV-madgraph | 17.43 | 50000 |
| RadionTohhTohbbhbb_narrow_M-2500_13TeV-madgraph | 6.646 | 50000 |
| RadionTohhTohbbhbb_narrow_M-3000_13TeV-madgraph | 1.519 | 50000 |

TABLE 3.3: List of radion $\rightarrow \text{HH} \rightarrow b\bar{b}$ Monte Carlo simulation and its corresponding cross section and the number of events. The cross sections are used in McM process at LO and not used in the final results.

| Samples | $\sigma(\text{pb})$ | Events |
|-------------------|---------------------|------------|
| QCD_HT-100to200 | 2.785×10^7 | 81,906,377 |
| QCD_HT-200to300 | 1.717×10^6 | 18,752,566 |
| QCD_HT-300to500 | 3.513×10^5 | 20,312,907 |
| QCD_HT-500to700 | 3.163×10^4 | 19,755,616 |
| QCD_HT-700to1000 | 6831 | 15,595,234 |
| QCD_HT-1000to1500 | 1207 | 4,966,123 |
| QCD_HT-1500to2000 | 119.9 | 3,964,488 |
| QCD_HT-2000toInf | 25.24 | 1,984,407 |

TABLE 3.4: List of multijet Monte Carlo simulation and its corresponding cross section and the number of events. The cross sections are used in McM process at LO.

3.3 Event Reconstruction and Selection

To reduce the impact from both cosmic particles and noise of calorimeters, missing transverse energy, MET, filters are applied. If all particles are detected and well-reconstructed in the detector, the sum of transverse momentum will be zero. However, if there are noise, ill-reconstructed particles or jets, the sum of transverse momentum will not equal to zero, and the negative of its value is defined as MET. The filters remove most events having anomaly MET based on different information given from the detectors. We require the event to pass all

| M_X (GeV) | $\sigma(pp \rightarrow X_G \rightarrow HH)$ (fb) | $\sigma(pp \rightarrow X_R \rightarrow HH)$ (fb) |
|-------------|--|--|
| 750 | 2.408 | 155.46 |
| 800 | 1.771 | 128.68 |
| 900 | 0.953 | 88.433 |
| 1000 | 0.559 | 62.057 |
| 1500 | 0.057 | 12.897 |
| 1800 | 0.018 | 5.6664 |
| 2000 | 9.03E-03 | 3.3868 |
| 2500 | 1.86E-03 | 1.0193 |
| 3000 | 3.03E-04 | 0.3280 |
| 3500 | 1.15E-04 | 0.1114 |
| 4500 | 8.91E-06 | 1.26E-02 |

TABLE 3.5: List of the cross section \times the branch ration of HH decay in fb. The model $k/\bar{M}_{Pl} = 0.1$ in bulk graviton is considered, and the model $\Lambda_R = 3\text{TeV}$ and $kl = 35$ of radion is considered.

filters listed in table 3.6[37].

| Triggers |
|---------------------------|
| primary vertex filter |
| beam halo filter |
| HBHE noise filter |
| HBHE iso noise filter |
| ECAL TP filter |
| ee badSC noise filter |
| Bad PF Muon Filter |
| Bad Charged Hadron Filter |

TABLE 3.6: List of MET filters applied in the analysis.

After passing MET filters, at least one reconstructed pp collision vertex which passes following criteria is required in an event.

- Number of degree of freedom > 4
- Absolute displacement from the beamspot position along the z direction $< 24\text{ cm}$

- Absolute displacement from the beamspot position along the transverse direction < 2 cm

For the final state is all-hadronic, lepton veto is implemented. The event will be vetoed either if there is a tight-tagged muon or electron, or if there are two loose-tagged mouns or electrons with opposite charged.

3.3.1 Higgs Jet Reconstruction

Each candidate of particles is reconstructed with Particle-Flow, PF, algorithm in CMS by all the detector components[38, 39]. In the algorithm, priority of reconstruction form high to low are: muons, electrons, photons, charged hadrons, and neutral hadrons.

The jets are clustered with anti- k_T algorithm by PF candidates[40]. Anti- k_T algorithm is done described below:

$$d_{ij} = \min(k_{ti}^{2p}, k_{tj}^{2p}) \frac{\Delta_{ij}^2}{R^2} \quad (3.1)$$

$$d_{iB} = k_{ti}^{2p},$$

where $\Delta_{ij}^2 = (y_i - y_j)^2 + (\phi_i - \phi_j)^2$, and k_{ti} , y_i , and ϕ_i are the transverse momentum, rapidity, and azimuth of particle i. The value of p is set according to the algorithm. The anti- k_T algorithm uses $p = -1$. Considering minimum term of k_t^{2p} between one hard particle and the selected soft particle compared to that between the soft particle and another soft particle, the former will be smaller because while the transverse momentum of hard particles is larger, its inverse square is smaller. Therefore, d_{ij} of the former is shorter, that is, a soft particle is more likely to cluster with hard particle around it. As a consequence, if there is no other hard particle within the range $2R$ of a hard particle, it will cluster a conical jet with all soft particles within range R . In other situation where the distance of two hard particles is between R and $2R$, one can show that the particle having larger transverse momentum will cluster a conical jet, while the other

is partly conical. Last, where distance of two hard particles $< R$, two particles will merge into single jet. In the analysis, the jets is clustered using anti- k_T with range parameter R set to 0.8 (refrred as AK8 jets).

In one bunch crossing, the vetex having highest energy called primary vertex, and the others are called pile-ups, PUs. PUs may contribute some components in jet clustering which do not originally belong to them. We can mitigate the effect by PUPPI algorithm[41], which is described below: First, a shape α_i of a particle i is defined:

$$\alpha_i = \log \sum_{j \in event} \xi_{ij} \times \Theta(\Delta R_{ij} - R_{min}) \times \Theta(R_0 - \Delta R_{ij}) \quad (3.2)$$

$$\xi_{ij} = \frac{p_{Tj}}{\Delta R_{ij}},$$

where Θ is the Heaviside step function, p_T is the transverse momentum, and ΔR_{ij} is the distance between particle i and j in $\eta\phi$ space. Hence, only particles falling in the cone size R_0 but not closer than R_{min} contribute to α . R_0 represent the locality of a jet, and R_{min} is most restricted by resolution of the detector. Then we seperate events into two cases: with and without tracker information. The former is used to weight the charged particles in central region, while the latter is used for charged particles in forward region and neutral particles. An addition scale factor depending on rapidity is applied to forward region. The calculation of weight uses the quantities of the median and the left-side RMS of α distribution. Finally, the weight of a particle is:

$$\chi_i^2 = \Theta(\alpha_i - \bar{\alpha}_{PU}) \frac{(\alpha_i - \bar{\alpha}_{PU})^2}{\sigma_{PU}^2}, \quad (3.3)$$

$$\omega_i = F_{\chi^2, NDF=1}(\chi_i^2),$$

where F_{χ^2} is the cumulative distribution function of the χ^2 distribution. One can find that if α of a particle less than the median, it will be considered from PU, and the step function in the first equation gives it a value of zero, while if α

greater than the median, the value of χ^2 is close to one.

Basic selection is applied on AK8 jet. We only consider the jets having the largest and the second largest transverse momentum in an event. The p_T of the jets must greater than 300 GeV and pseudorapidity $|\eta|$ must less than 2.4. Also, the tight PF jet identification provided by JETMET group is required[42], which is summarized in the table 3.7, where fraction are referring to energy fraction, and constituents and multiplicity are referring to the number of particles.

| Variable | Cut |
|-------------------------|-------|
| Neutral hadron fraction | < 0.9 |
| Neutral EM fraction | < 0.9 |
| Charged EM fraction | < 0.9 |
| Number of Constituents | > 1 |
| Muon fraction | < 0.8 |
| Charged hadron fraction | > 0 |
| Charged Multiplicity | > 0 |

TABLE 3.7: List of the tight PF jet identification.

3.3.2 Heavy Resonance Selection

The difference between two $|\eta|$ of two leading jets of signal events will be less than that of multi-jet events because the Higgs jets are from heavy resonance decay resulting in two jets close to each other, and yet the $|\eta|$ of the jets in multi-jet events are uniformly distributed. To reduce the contribution from multi-jet events, which are our mainly source of background, we require a $|\Delta\eta|$ cut on < 1.3 . Next, We target the heavy resonances whose mass is above 800 GeV. Therefore, a revised mass of heavy resonances is also required. The mass of heavy resonances, M_{jj} , is get from sum of four momenta of two Higgs jets. A revised mass is used to narrow the width and correct the peak position of the

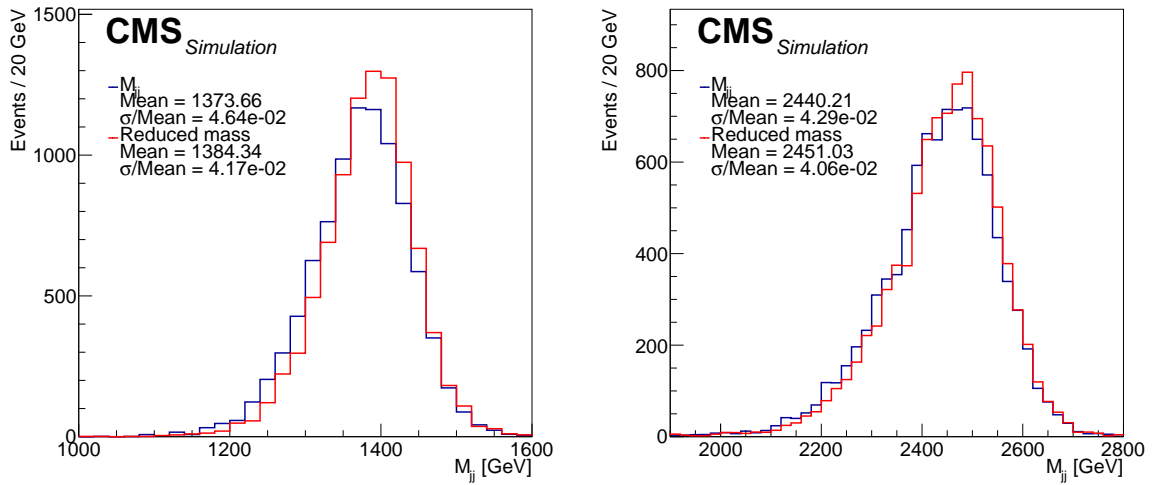


FIGURE 3.1: The comparison of M_{jj} and reduced mass distribution of bulk graviton $M_X = 1.4$ (left) and 2.5 TeV (right). The mean and the σ/mean of a Gaussian fit to the distribution are shown.

M_{jj} distribution, referred as "reduced mass" for the following chapters.

$$M_{jj}^{reduced} = M_{jj} - (M_{j1} - M_H) - (M_{j2} - M_H), \quad (3.4)$$

where M_{j1} or M_{j2} is the mass of Higgs jets, and M_H is the mass of physic Higgs boson. The reduce mass is required to be greater than 750 GeV.

3.3.3 Higgs Tagging Selection

The soft-drop procedure is implemented to re-cluster the jet by removing soft contribution as follow[43]

- Deculster a targeted jet into two sub-jets.
- Continue to decompose the sub-jets until the condition is achieved

$$\frac{\min(p_{T1}, p_{T2})}{p_{T1} + p_{T2}} > Z_{cut} \times \left(\frac{\Delta R_{12}}{R_0}\right)^\beta, \quad (3.5)$$

where R_0 is the cone size of the original cluster algorithm, p_T are the transverse momenta of two sub-jets, ΔR_{12} is the distance of two sub-jets in $\eta\phi$ space, and Z_{cut} and β are parameters.

- The unsplit singlet particle at the end will either be removed or remain preserved.

If $\beta > 0$, the soft contribution is removed while remain a fraction of soft-collinear radiation. If $\beta < 0$, soft drop removes both soft and collinear radiation. In CMS, the Z_{cut} and β are set 0.1 and zero respectively. The difference between the mean of the distribution of mass of PUPPI soft-drop jets and the mass of physical Higgs boson is found[44]. A Correction is applied to move the peak to the true physical value. The ratio is derived by peak of the mass distribution of reconstructed jets in WW dijet Monte Carlo simulations to mass of true physical value. The corrected PUPPI soft-drop mass of the first two leading jets are required between 105 and 135 GeV, which has been optimized.

The ratio τ_N to τ_{N-1} is used as a discriminant to separate the boosted events decaying into N particles from multi-jet events. τ_N is so-called "N-subjettiness" algorithm[45–47]

$$\tau_N = \frac{1}{d_0} \sum_k p_{T,k} \min\{\Delta R_{1,k}, \Delta R_{2,k}, \dots, \Delta R_{N,k}\} \quad (3.6)$$

$$d_0 = \sum_k p_{T,k} R_0,$$

where k runs over the constituent particles in a given jet, ΔR_{jk} is the distance between particle j and k in $\eta\phi$ space, R_0 is the cone size of the original cluster algorithm. In the analysis, the boosted jets are decaying into two sub-jets, so τ_2 to τ_1 ratio is used, and it is referred as τ_{21} in the following chapters. The τ_{21} is required to be less than 0.55. The working point and simulation-to-data scale factor is derived by JME POG[48].

The double-b tagger is a multiple variable analysis discriminant used to identify b-flavor jets[49]. Jets in multi-jet events and Higgs jets decaying into $b\bar{b}$ are used for training. Here lists out the input information:

- The first four impact parameters to its uncertainty values ordered from the largest to the smallest.
- The N-subjettiness axes referred as τ -axes use the information of N-subjettiness
- The first two impact parameters to its uncertainty values of τ -axes ordered from the largest to the smallest.
- The measured significance of impact parameters of the first two tracks whose mass of secondary vertex is above bottom quark threshold.
- The number of secondary vertices of the jet.
- The significance of two dimensional distance between the primary vertex and the secondary vertex and flight distance of the secondary vertex with smallest three dimensional distance uncertainty for each τ -axes.
- ΔR of the two secondary vertices with smallest three dimensional distance uncertainty for each τ -axes.
- The τ -axis of the two secondary vertices with smallest three dimensional distance uncertainty for each τ -axes.
- The sum of the mass of the secondary vertices associated to the τ -axis for each τ -axes.
- The sum of energy of secondary vertices associated to the τ -axis for each τ -axes.
- The relative pseudorapidity of three tracks of leading secondary vertex with respect to their τ -axis for each τ -axes.

- The sum of energy of all tracks in the AK8 jet.
- The z variable, defined as:

$$z = \Delta R(SV_0, SV_1) \times \frac{p_{T,SV_1}}{m(SV_0, SV_1)}, \quad (3.7)$$

where SV_0 and SV_1 are the secondary vertexes with the smallest 3D flight distance uncertainty.

The double-b working points and simulation-to-data scale factor is derived by BTV POG[50]. The analysis is separated into two categories with two Higgs jets in the events either both passing loose working point (> 0.3) or both passing tight working point (> 0.8), which are referred as LL and TT categories respectively. The events in TT region will be excluded from LL region to make two categories orthogonal.

3.4 Triggers

Since the final state includes di-Higgs jets, the triggers are selected considering the requirements on the scale sum of the energy of external partons H_T , $|\Delta\eta|$ (the first two leading jets), M_{jj} , p_T , the groomed mass of the jets, and double-b tagger. PFHT900 is used to supplement the inefficiency of PFHT800 in period H of data taking.

| Triggers |
|--|
| HLT_PFHT800 |
| HLT_PFHT900 |
| HLT_PFHT650_WideJetMJJ900DEtaJJ1p5 |
| HLT_AK8PFJet360_TrimMass30 |
| HLT_AK8DiPFJet280_200_TrimMass30_BTagCSV_p20 |
| HLT_AK8PFHT650_TrimR0p1PT0p03Mass50 |

TABLE 3.8: List of Triggers applied in the analysis.

| Selection | Requirement |
|--------------------------------|--|
| Number of good vertex | > 1 |
| MET Filters | AND of all filters |
| Trigger | OR of all triggers |
| Lepton veto | one tight-tagged or two loose-tagged |
| p_T of AK8 jets | $> 300\text{GeV}$ |
| $ \eta $ of AK8 jets | < 2.4 |
| Tight LepVeto jet ID | pass |
| $ \Delta\eta$ (two AK8 jets) | < 1.3 |
| Reduce mass | $> 750\text{ GeV}$ |
| corrected PUPPI soft-drop mass | $105\text{GeV} < \text{and} < 135\text{GeV}$ |
| τ_{21} | < 0.55 |
| double-b tagger | > 0.3 (LL) or > 0.8 (TT) |

TABLE 3.9: List of all selection in the analysis.

| M_X | Trig. | Jet p_T, η | Veto _{lept} | $\Delta\eta$ | Lepton | τ_{21} | M_{AK8} | M_{jj}^{red} | LL | TT |
|-------|-------|-----------------|----------------------|--------------|--------|-------------|-----------|----------------|-------|-------|
| 750 | 0.432 | 0.248 | 0.247 | 0.213 | 0.213 | 0.093 | 0.029 | 0.024 | 0.016 | 0.009 |
| 800 | 0.547 | 0.367 | 0.367 | 0.327 | 0.326 | 0.152 | 0.051 | 0.050 | 0.036 | 0.021 |
| 900 | 0.693 | 0.552 | 0.552 | 0.487 | 0.485 | 0.245 | 0.083 | 0.083 | 0.061 | 0.033 |
| 1000 | 0.772 | 0.666 | 0.666 | 0.552 | 0.550 | 0.296 | 0.101 | 0.101 | 0.075 | 0.041 |
| 1200 | 0.859 | 0.792 | 0.792 | 0.585 | 0.584 | 0.335 | 0.116 | 0.116 | 0.084 | 0.044 |
| 1400 | 0.902 | 0.854 | 0.854 | 0.591 | 0.590 | 0.355 | 0.123 | 0.123 | 0.087 | 0.044 |
| 1600 | 0.928 | 0.890 | 0.889 | 0.592 | 0.591 | 0.358 | 0.124 | 0.124 | 0.086 | 0.041 |
| 1800 | 0.946 | 0.913 | 0.913 | 0.595 | 0.594 | 0.365 | 0.124 | 0.124 | 0.082 | 0.036 |
| 2000 | 0.957 | 0.931 | 0.931 | 0.598 | 0.598 | 0.365 | 0.127 | 0.127 | 0.081 | 0.036 |
| 2500 | 0.975 | 0.956 | 0.955 | 0.596 | 0.595 | 0.367 | 0.125 | 0.125 | 0.076 | 0.030 |
| 3000 | 0.981 | 0.966 | 0.965 | 0.589 | 0.589 | 0.357 | 0.123 | 0.123 | 0.068 | 0.022 |
| 3500 | 0.987 | 0.973 | 0.972 | 0.582 | 0.582 | 0.349 | 0.116 | 0.116 | 0.059 | 0.018 |
| 4500 | 0.991 | 0.977 | 0.976 | 0.579 | 0.578 | 0.334 | 0.103 | 0.103 | 0.044 | 0.010 |

TABLE 3.10: The cut flow of all M_X (GeV) of spin-0 radion.

3.5 Simulation Distribution

In the section, distribution of Monte Carlo simulations of signal and background will be shown to demonstrate the discrimination of each variables of the selection. For each distribution, all selection described in previous section is required

| M_X | Trig. | Jet p_T, η | Jet ID | $\Delta\eta$ | Veto _{lep} | τ_{21} | M_{AK8} | M_{jj}^{red} | LL | TT |
|-------|-------|-----------------|--------|--------------|---------------------|-------------|-----------|----------------|-------|-------|
| 750 | 0.610 | 0.368 | 0.368 | 0.331 | 0.330 | 0.149 | 0.049 | 0.039 | 0.027 | 0.015 |
| 800 | 0.758 | 0.541 | 0.541 | 0.503 | 0.502 | 0.237 | 0.080 | 0.079 | 0.057 | 0.032 |
| 900 | 0.903 | 0.772 | 0.771 | 0.716 | 0.715 | 0.371 | 0.125 | 0.124 | 0.092 | 0.051 |
| 1000 | 0.958 | 0.885 | 0.885 | 0.801 | 0.799 | 0.434 | 0.151 | 0.151 | 0.111 | 0.062 |
| 1200 | 0.988 | 0.962 | 0.961 | 0.843 | 0.842 | 0.499 | 0.178 | 0.178 | 0.129 | 0.068 |
| 1400 | 0.996 | 0.984 | 0.983 | 0.854 | 0.853 | 0.524 | 0.182 | 0.182 | 0.129 | 0.064 |
| 1600 | 0.998 | 0.993 | 0.993 | 0.858 | 0.857 | 0.532 | 0.186 | 0.186 | 0.128 | 0.061 |
| 1800 | 0.999 | 0.996 | 0.996 | 0.864 | 0.863 | 0.543 | 0.193 | 0.193 | 0.130 | 0.059 |
| 2000 | 1.000 | 0.998 | 0.998 | 0.861 | 0.860 | 0.541 | 0.190 | 0.190 | 0.123 | 0.054 |
| 2500 | 1.000 | 0.999 | 0.999 | 0.862 | 0.862 | 0.538 | 0.188 | 0.188 | 0.113 | 0.044 |
| 3000 | 1.000 | 1.000 | 0.999 | 0.865 | 0.865 | 0.530 | 0.186 | 0.186 | 0.102 | 0.034 |
| 4000 | 1.000 | 1.000 | 0.999 | 0.861 | 0.861 | 0.505 | 0.166 | 0.166 | 0.078 | 0.021 |
| 4500 | 1.000 | 1.000 | 0.999 | 0.859 | 0.858 | 0.502 | 0.156 | 0.156 | 0.065 | 0.016 |

TABLE 3.11: The cut flow of all M_X (GeV) of spin-2 bulk graviton.

except the variable itself and double-b tagger discriminant. The cross section of every signal is set to 20 pb. The numbers of events of signal and of background are normalized to same luminosity of data of 35.9fb^{-1} . Multi-jet events are added up by samples of different H_T section listed in table 3.4, and separated into four categories summarized in the table 3.10. Besides, the cross sections at leading order of multi-jet events are multiplied by a factor about 0.7 to modify them closer to the value of next leading order.

| category | hadron flavor of AK8 jets | hadron flavor of subjets |
|----------|---------------------------|--------------------------|
| bb | 5 | 5 (both) |
| b | 5 | 5 (only one) |
| cc/c | 4 | 4 (at least one) |
| light | all remaining | all remaining |

TABLE 3.12: List of categorization of multijet events.

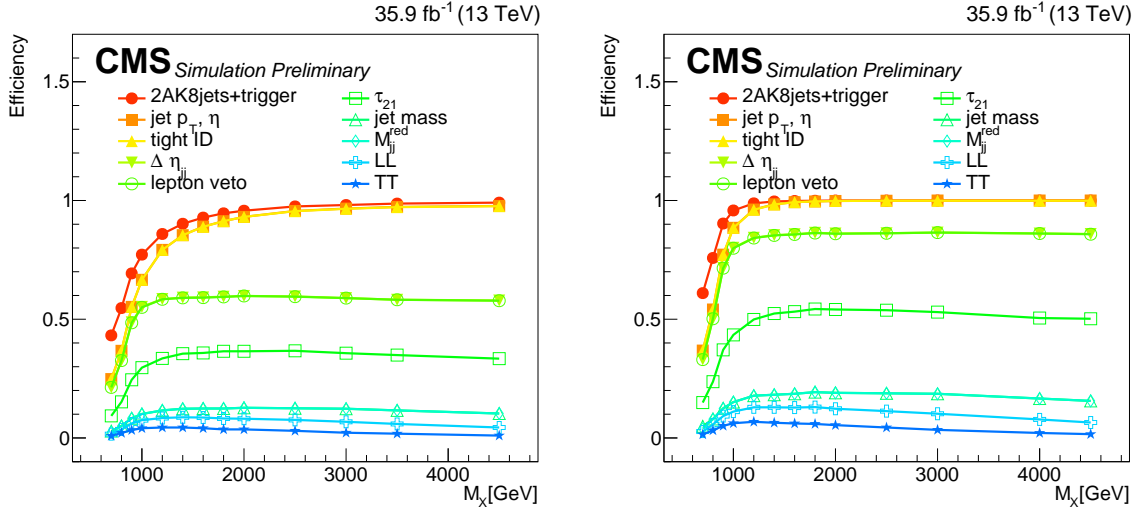


FIGURE 3.2: The cut flow of all M_X (GeV) of spin-0 radion (left) and of spin-2 bulk graviton (right).

3.6 Data and Monte Carlo Comparison

In the section, the comparison of Monte Carlo simulations of background and data will be shown to demonstrate the dominant components in data. Multi-jet events are added up by samples of different H_T section listed in table 3.4, and separated into four categories summarized in the table 3.10. Besides, the cross sections at leading order of multi-jet events are multiplied by a factor about 0.7 to modify them closer to the value of next leading order.

- Pile-up re-weighting: all selection is used except τ_{21} and double-b tagger. The weighting procedure is described in chapter 2.2.
- Inverse double-b region : all selection is used except only one of double-b taggers passing the loose criteria.
- Inverse τ_{21} region: all selection is used except only one of τ_{21} passing the criteria of 0.55.

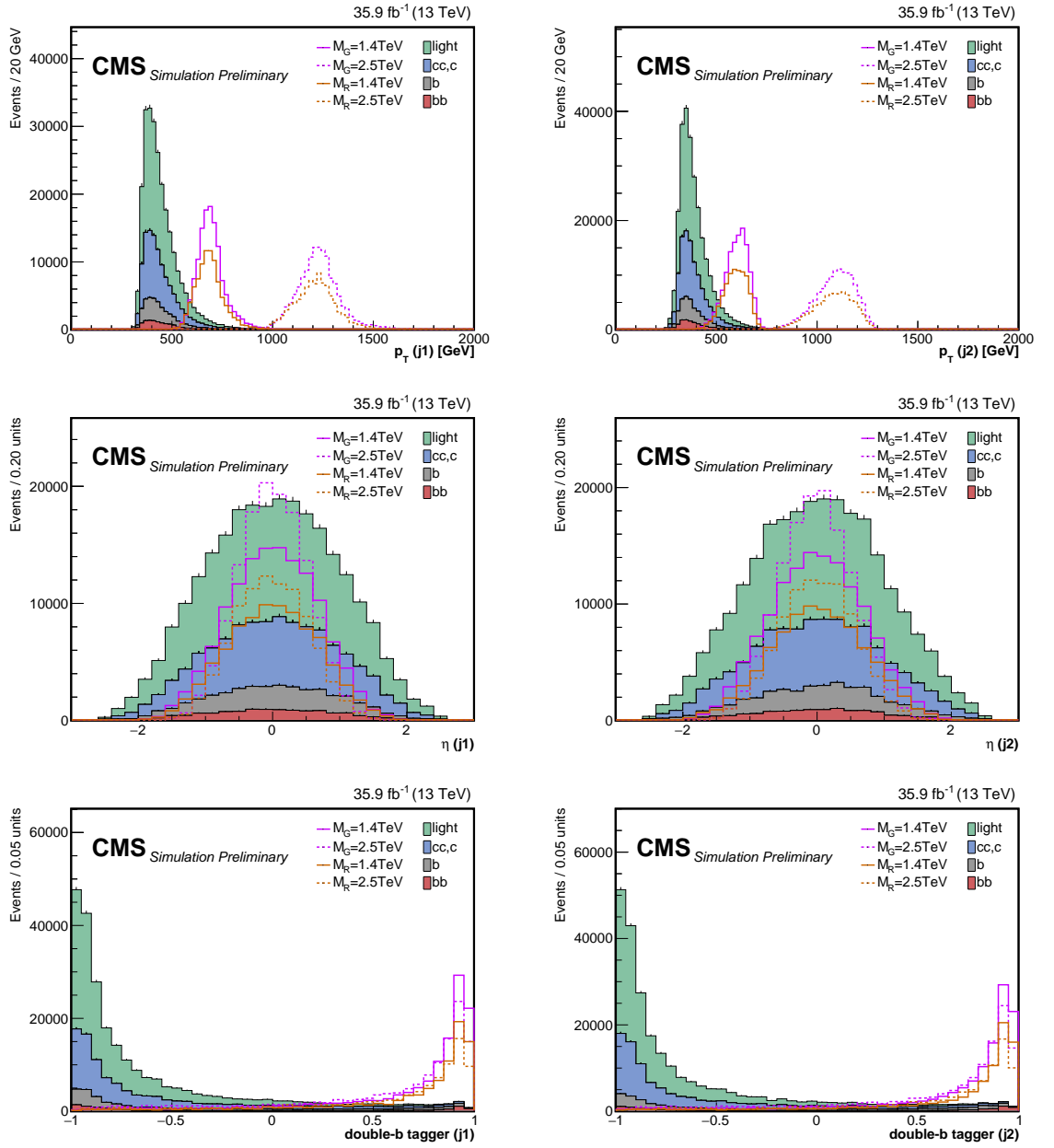


FIGURE 3.3: The comparison of signal and background. The signals of $M_X = 1.4$ TeV and 2.5 TeV from both models are shown. The cross section is set to 20 pb in the figures. Multi-jet events are separated into four categories summarized in the table 3.10. From top to bottom are the comparison of p_T , η , and double-b tagger of leading (left) and next leading (right) AK8 jet.

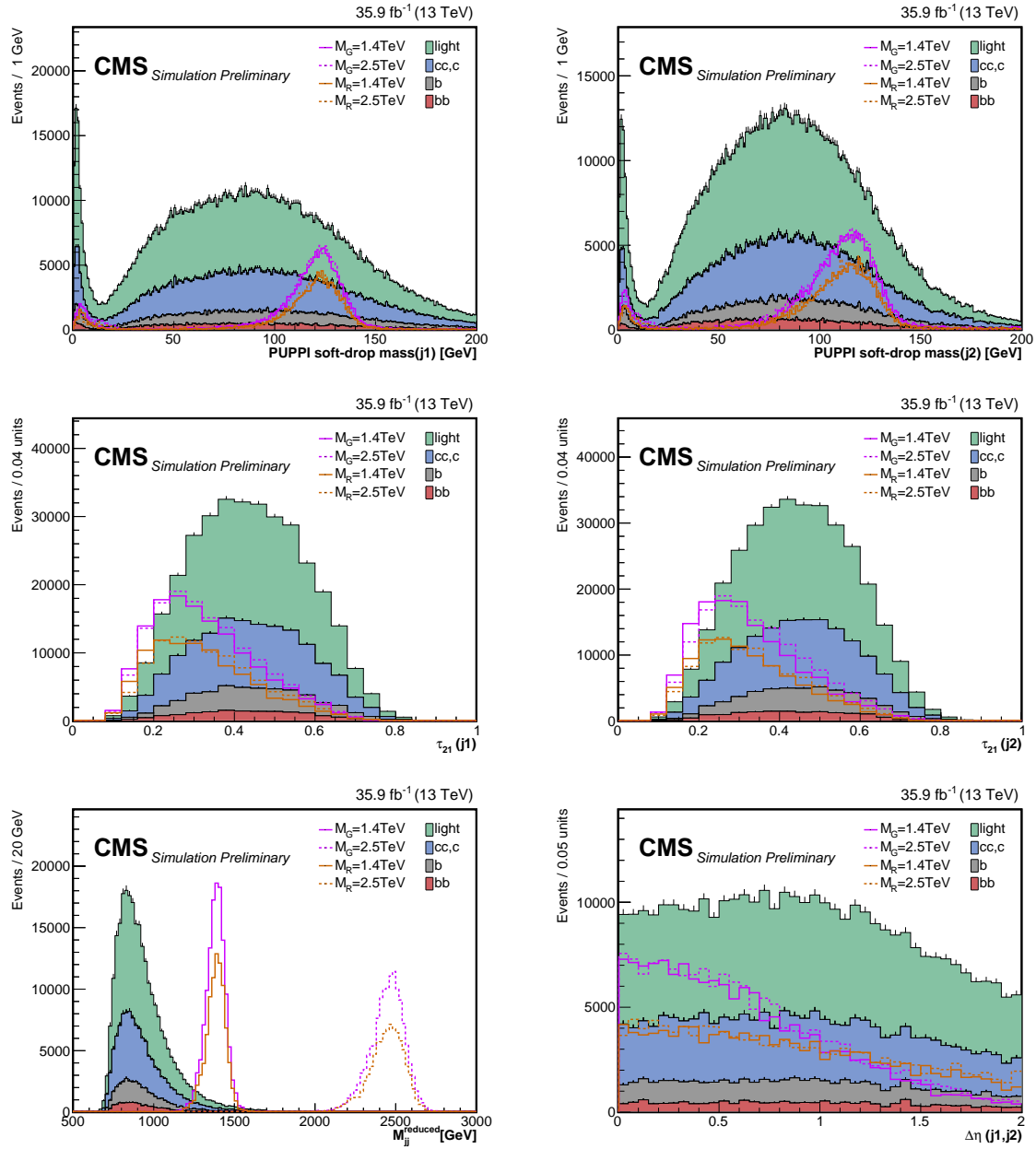


FIGURE 3.4: The comparison of signal and background. The signals of $M_X = 1.4$ TeV and 2.5 TeV from both models are shown. The cross section is set to 20 pb in the figures. Multi-jet events are separated into four categories summarized in the table 3.10. From top to bottom are the comparison of PUPPI soft-drop mass, τ_{21} of leading (left) and next leading (right) AK8 jet, the reduced mass (bottom left), and $|\Delta\eta$ (the two leading AK8 jets)| (bottom right).

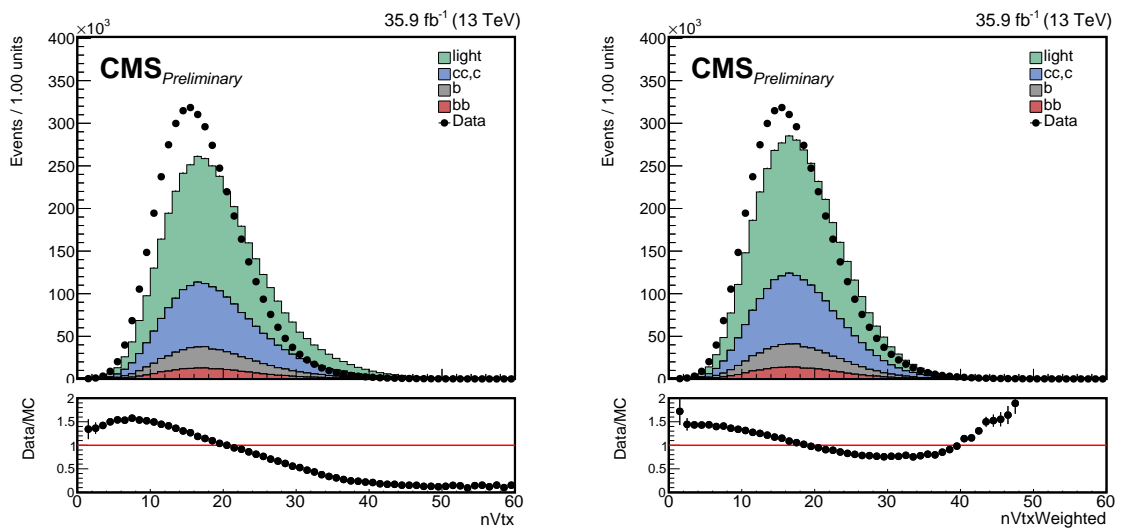


FIGURE 3.5: The comparison of data and background of pile-up distribution with (left) and without (right) pile-up re-weighting. Multi-jet events are separated into four categories summarized in the table 3.10.

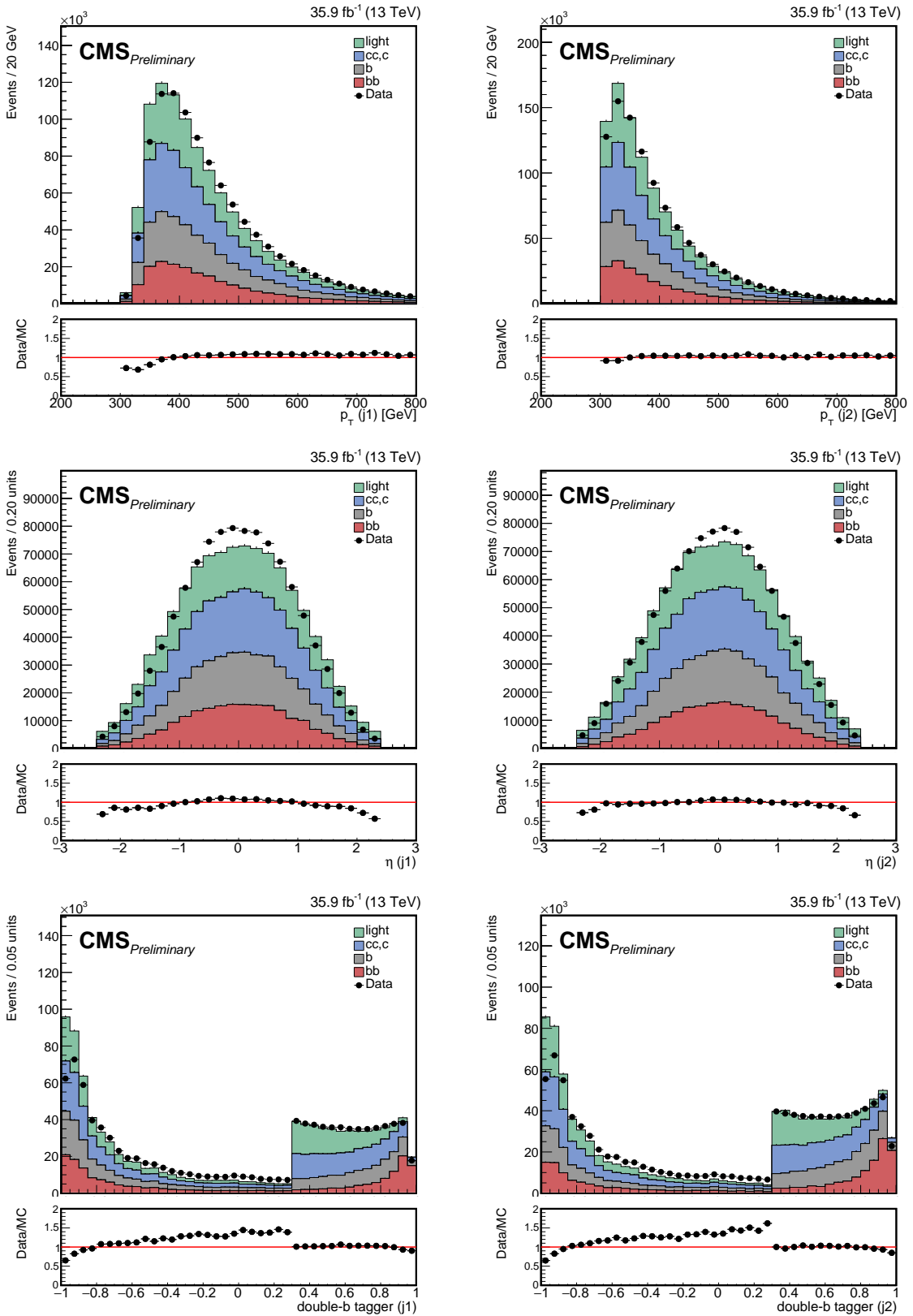


FIGURE 3.6: The comparison of data and background in inverse double-b region. Multi-jet events are separated into four categories summarized in the table 3.10. From top to bottom are the comparison of p_T , η , and double-b tagger of leading (left) and next leading (right) AK8 jet.

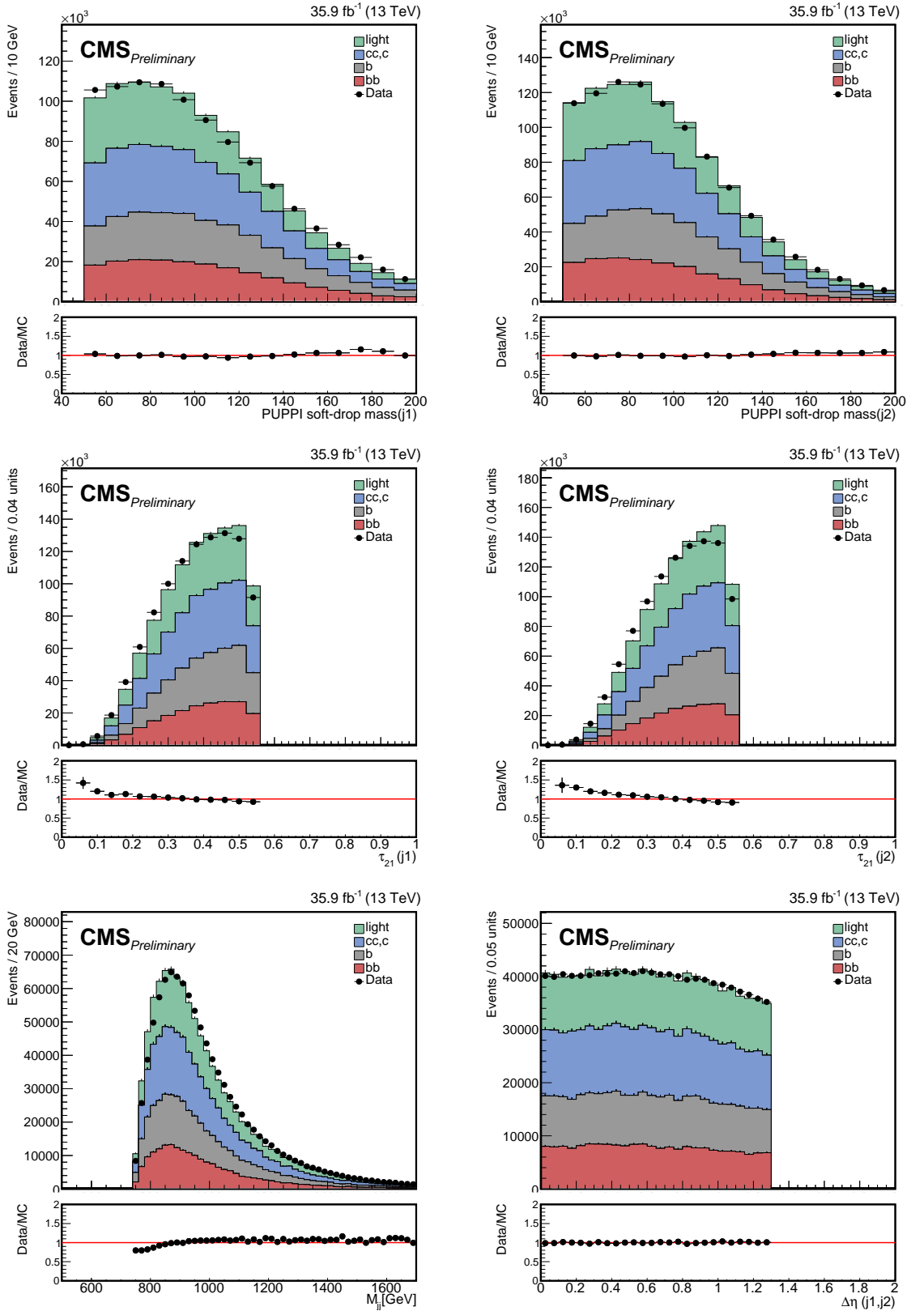


FIGURE 3.7: The comparison of data and background in inverse double-b region. Multi-jet events are separated into four categories summarized in the table 3.10. From top to bottom are the comparison of PUPPI soft-drop mass, τ_{21} of leading (left) and next leading (right) AK8 jet, the reduced mass (bottom left), and $|\Delta\eta|$ (the two leading AK8 jets) (bottom right).

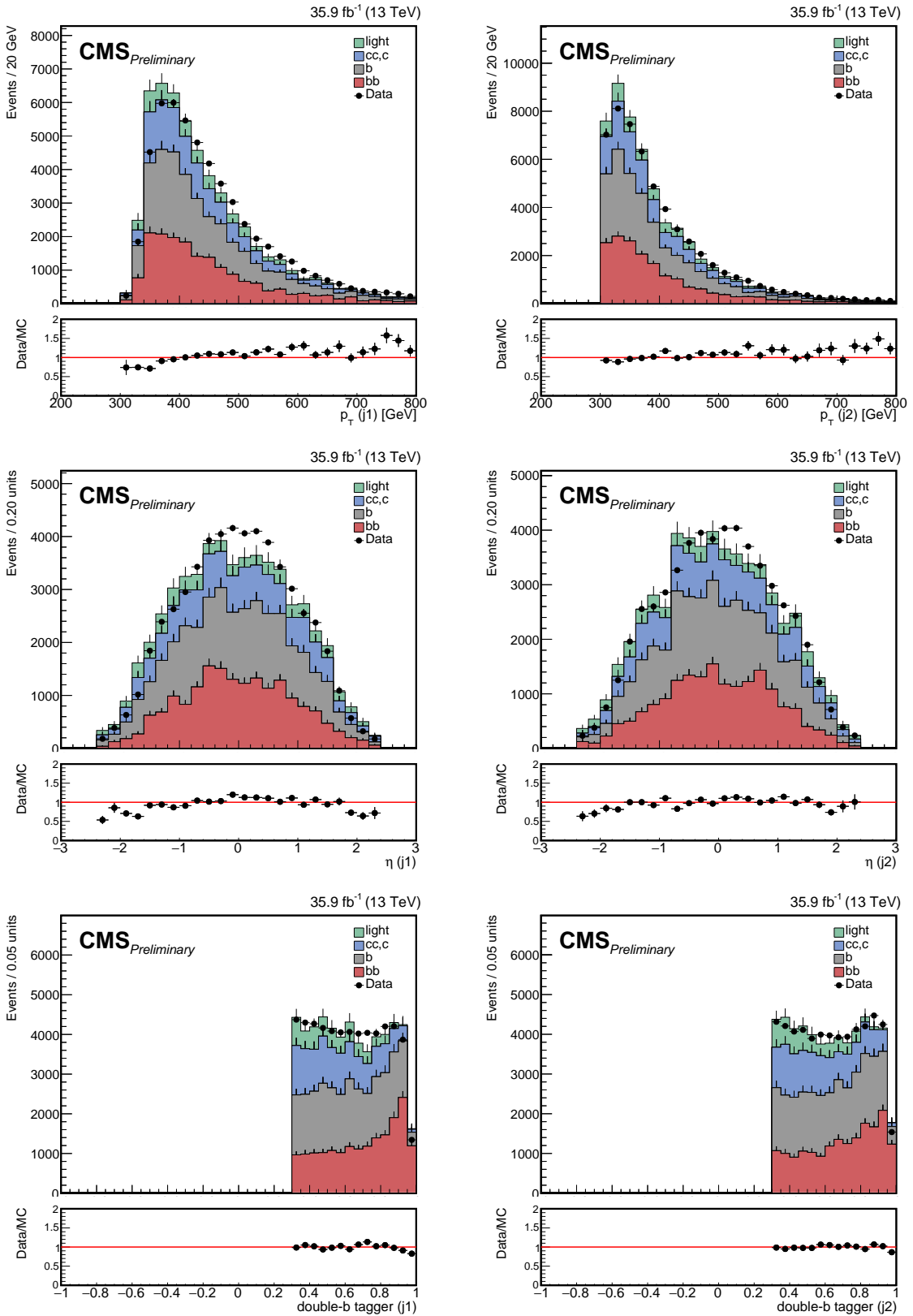


FIGURE 3.8: The comparison of data and background in inverse τ_{21} region. Multi-jet events are separated into four categories summarized in the table 3.10. From top to bottom are the comparison of p_T , η , and double-b tagger of leading (left) and next leading (right) AK8 jet.

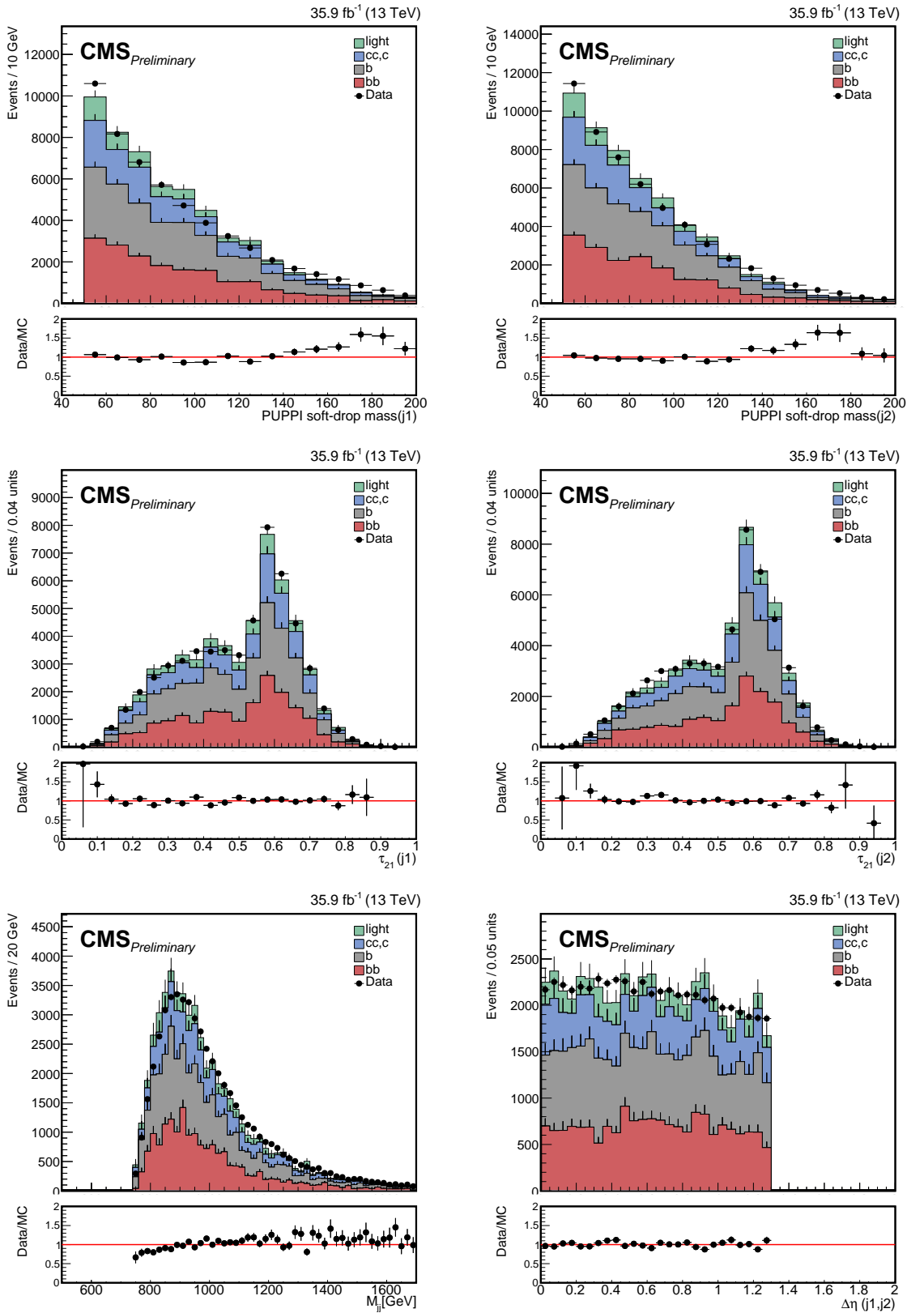


FIGURE 3.9: The comparison of data and background in inverse τ_{21} region. Multi-jet events are separated into four categories summarized in the table 3.10. From top to bottom are the comparison of PUPPI soft-drop mass, τ_{21} of leading (left) and next leading (right) AK8 jet, the reduced mass (bottom left), and $|\Delta\eta|$ (the two leading AK8 jets) (bottom right).

Chapter 4

Background Estimation

In this channel whose final state is four b-flavor jets, main background contribution comes from multi-jet events. The background estimation in the study combines two methods used in 2015 research: alphabet and bump hunt into alphabet assisted bump hunt[51].

4.1 Bump Hunt

The concept of searches for heavy resonance can be seen directly as finding a bump on the top of the smooth background, which is shown in figure 4.1. The fitted target is the mass spectrum of heavy resonances. The probability density functions used in fitting are level-exponential function for data and Gaussian for signal.

4.2 Alphabet

Alphabet method evolved from ABCD method which assumes the background is homogeneously distributed on the two-dimension histogram. The histogram is separated into signal region and sideband region. The background in signal region can be extrapolated from sideband region. For example, if we see the

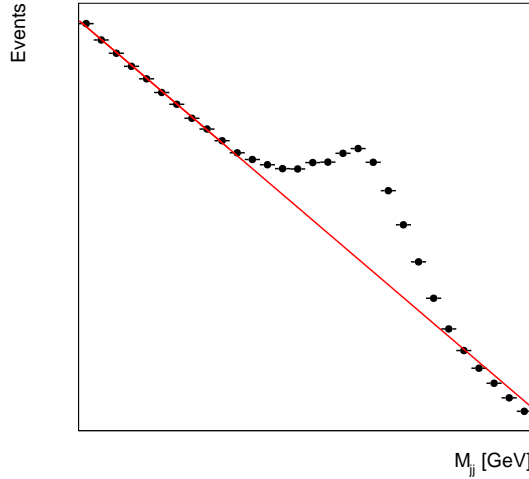


FIGURE 4.1: The cartoon of a bump on the background.

figure 4.2, the number of events in signal region can get by:

$$\begin{aligned}
 \frac{N_{signal}}{N_{anti-tag}} &= \frac{N_{sidebandB}}{N_{sidebandA}} = \frac{N_{sidebandD}}{N_{sidebandC}}, \\
 N_{signal} &= \frac{N_{sidebandB} \times N_{anti-tag}}{N_{sidebandA}} = \frac{N_{sidebandD} \times N_{anti-tag}}{N_{sidebandC}} \\
 &= N_{anti-tag} \times R_{p/f},
 \end{aligned} \tag{4.1}$$

where N is the number of events located in the region of square shape. The ratio $\frac{N_{signal}}{N_{anti-tag}}$ is referred as $R_{p/f}$ in the section. If the $R_{p/f}$ has dependence on the mass of the leading AK8 jet, one should use Alphabet method instead of ABCD method, as figure 4.3 and 4.4 show. Alphabet method gives $R_{p/f}$ a dependence on the mass of the leading AK8 jet:

$$N_{signal} = N_{anti-tag} \times R_{p/f}(M_{leadingAK8}). \tag{4.2}$$

The $R_{p/f}$ is derived in each bin of the mass of leading AK8 jet in mass side band. All $R_{p/f}$ of each bin is fitted together by a quadratic polynominal fit to interpolate the $R_{p/f}$ in the region of mass of signal. The fit results are shown in figure 4.4. Finally, the predicted background is get from filling anti-tagged events weighted according to the mass of its leading AK8 jet. Figure 4.5 is predicted background

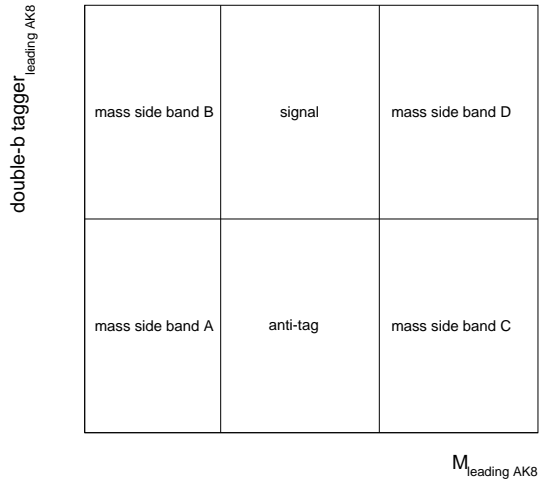


FIGURE 4.2: The cartoon of a two dimensional distribution.

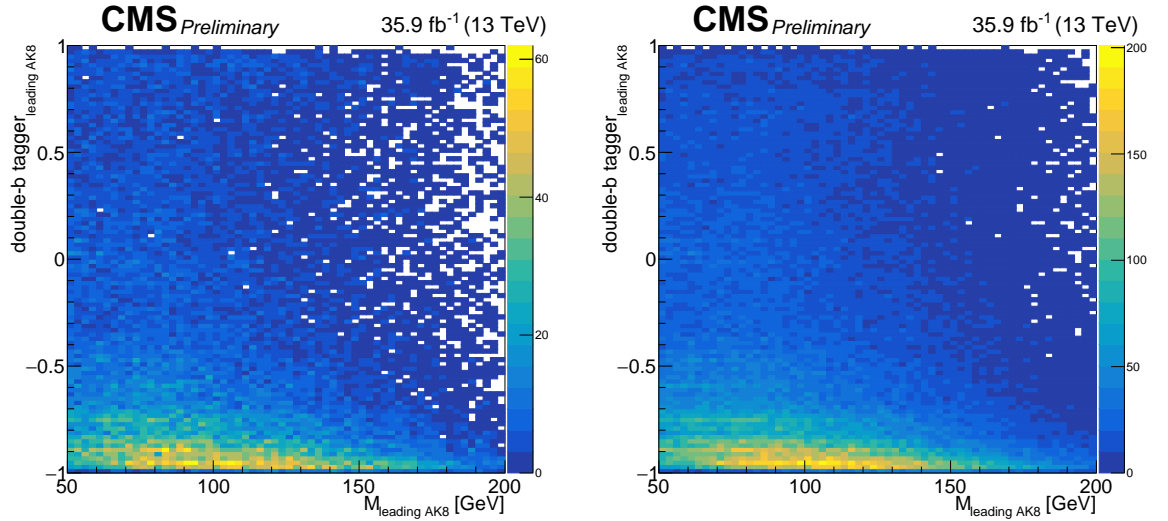


FIGURE 4.3: The double-b tagger versus the mass of the leading AK8 jet distribution in TT (left) and LL (right) region.

in both LL and TT region.

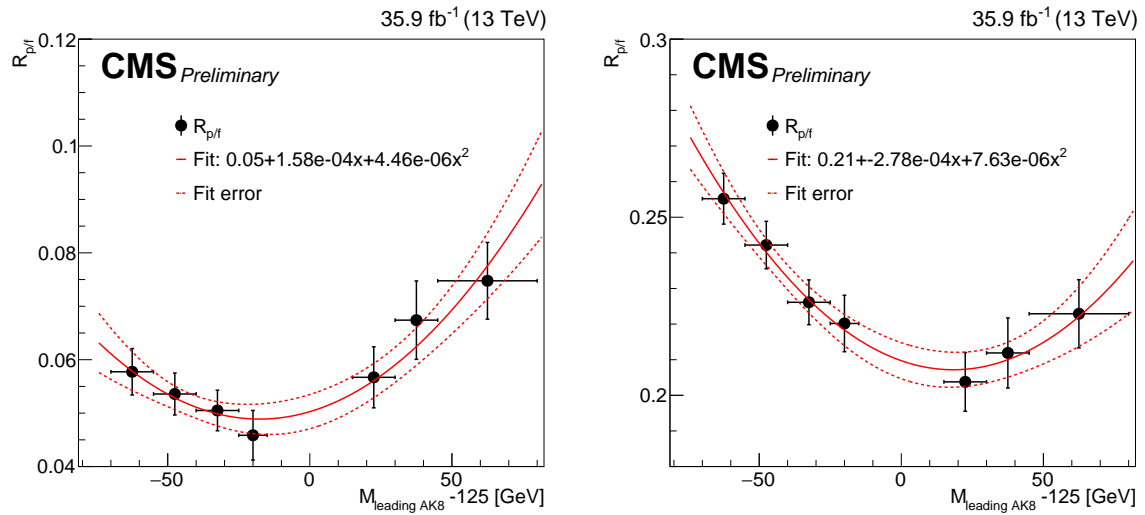


FIGURE 4.4: The $R_{p/f}$ and its quadratic fit in TT (left) and LL (right) region.

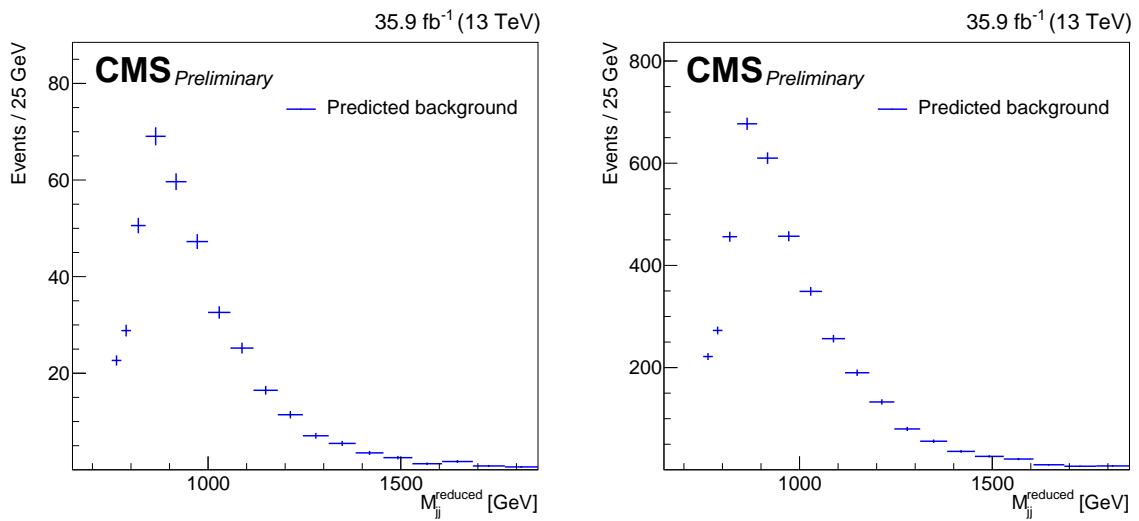


FIGURE 4.5: The predicted background from data in TT (left) and LL (right) region.

4.3 Alphabet Assisted Bump Hunt

The two background estimation methods, alphabet and bump hunt, use orthogonal information from data. While bump hunt drives in signal region, alphabet extrapolates from data in side band region. Therefore, we can combine two method into alphabet assisted bump hunt. The estimation is implemented as follow:

- Define a tagging and anti-tagging region. The double-b tagger working point is used as a discriminator here.
- Derive the ratio of number of events in tagging region to that of anti-tagging region, which referred below " $R_{p/f}$ ".
- The dependence of $R_{p/f}$ on M_{jj} and that on $M_{Higgs,Jet}$ are considered, while the latter is small enough to be ignored. The shape and the number of estimated background can be get from:

$$Bkg(M_{jj}) = R_{p/f}(M_{jj}) \times Anti-tag(M_{jj}), \quad (4.3)$$

which can be further reduced to

$$R_{p/f}(M_{jj}) = 1 + (M_{jj} \times lin_{par}) \quad (4.4)$$

$$Bkg(M_{jj}) = (1 + (M_{jj} \times lin_{par})) \times Anti-tag(M_{jj}),$$

where $Bkg(M_{jj})$ is not get from the p.d.f of Anti-tag, rather it get from fitting to the histogram of reduced mass in signal region directly. The parameters in the p.d.f of Anti-tag(M_{jj}) share the same parameters of $Bkg(M_{jj})$, and lin_{par} is a parameter of the linear dependence on M_{jj} . The initialized p.d.f is referred as pre-fit.

- The parameters of the p.d.f. of $Bkg(M_{jj})$ are retrained. The p.d.f. of Anti-tag(M_{jj}) is fitted to the histogram of reduced mass in anti-tagged region.

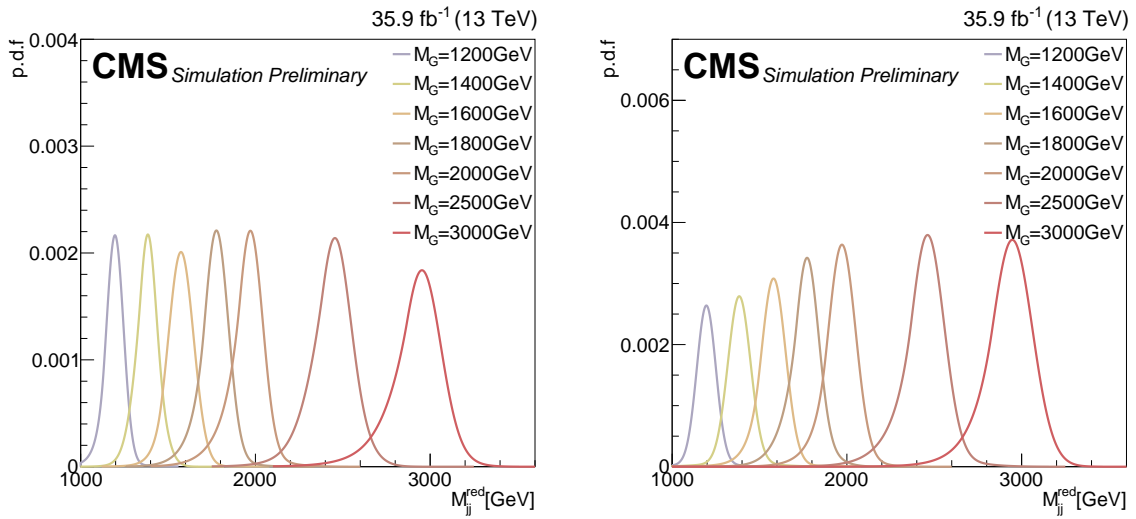


FIGURE 4.6: The p.d.f. of signal model in TT (left) and LL (right) category. The signal of Bulk graviton is used. The p.d.f.s are normalized to integral of all probability of one.

As both p.d.f. share the same parameters, the p.d.f. of $\text{Bkg}(M_{jj})$ is changed using the value of the parameters of $\text{Anti-tag}(M_{jj})$ to finish a post-fit procedure.

4.3.1 Signal model

The signal model is a combination of Gaussian and Crystal ball p.d.f. with the same mean. The p.d.f.s fitted to the signal are shown in figure 4.6.

4.3.2 Background model

The background model is chosen to describe the exponential-decay distribution of the reduced mass. Therefore, levelled exponential p.d.f. is used to fit to the shape. There is little difference between the form of the p.d.f used for signal region and for anti-tagged region. The p.d.f.s after fitted to the

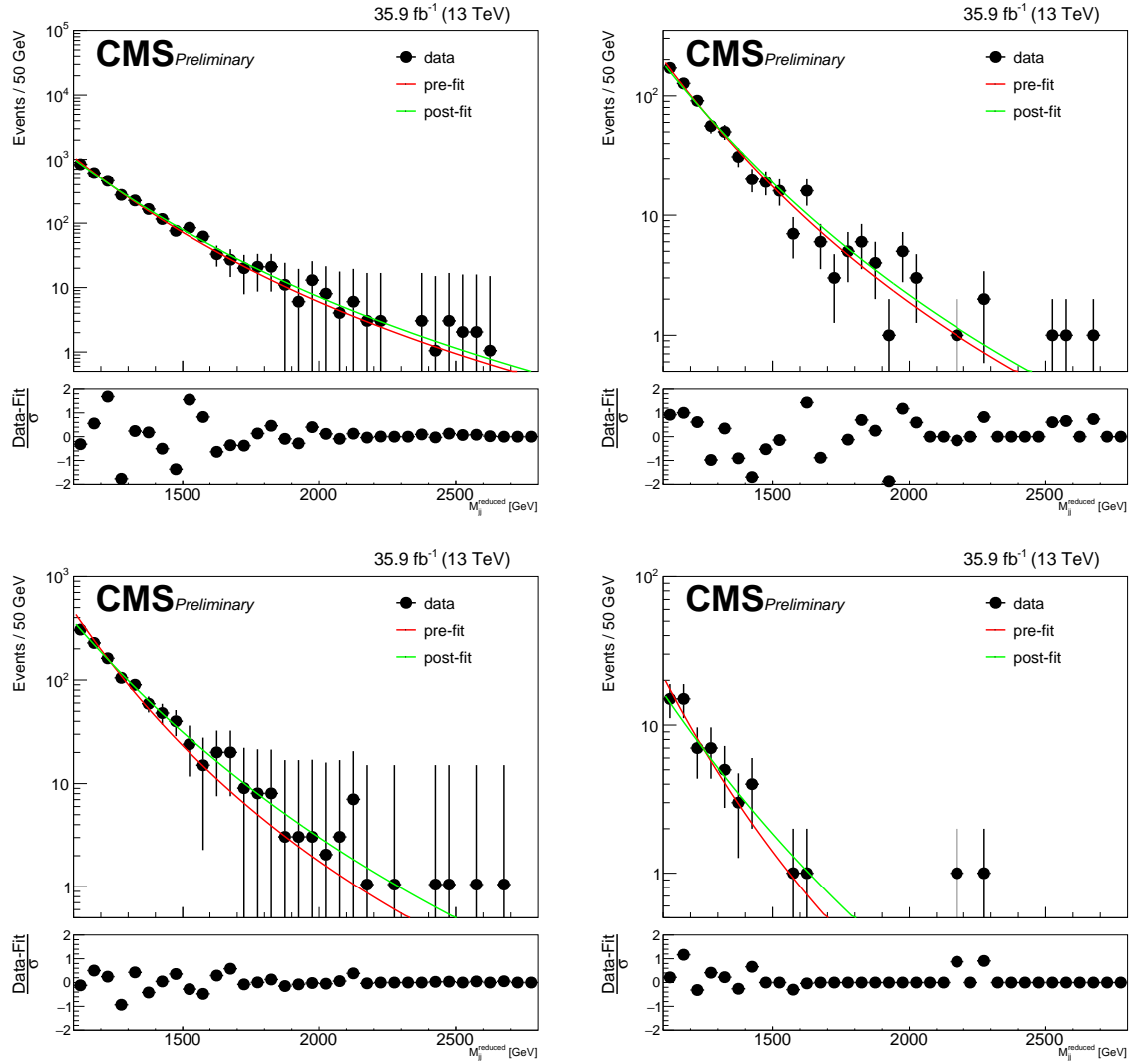


FIGURE 4.7: The pre-fit and post-fit on the data in anti-tag region (left) and signal region (right) in LL category (top) and TT category (bottom).

histogram in the pre-fit and post-fit procedure are shown in the figure 4.7.

$$\begin{aligned}
 Bkg_{sig} &= N \times (1 + lin \times M_{jj}^{red}) e^{\frac{M_{jj}^{red} \times p1}{1 + M_{jj}^{red} \times p1 \times p2}}, \\
 Bkg_{anti} &= N \times e^{\frac{M_{jj}^{red} \times p1}{1 + M_{jj}^{red} \times p1 \times p2}},
 \end{aligned} \tag{4.5}$$

Chapter 5

Systematic Uncertainty

5.1 Systematic Uncertainty on Signal Selection

- Luminosity: Intergrated luminosity is estimated with 2.5% uncertainty[52].
- Pile-ups: Pile-up efficiecy scale factor is applied to simulation weight the pile-up distribution as that of data. The pile-up distribution of data is measured by assuming minibias cross section equals to 69.2 mb, which has 4.6% uncertainty.
- Higgs tagging: Since there is no pure Higgs events in data, we cannot obtain the scale factor of Higgs-get tagging using the data. Instead, the Higgs-tagged uncertainty is measured by Higgs-jets and W-jets from simulation. The difference in mass scale and their jet flavor composition lead to different hadron shower response. Two shower and hadronization models is used to see how the hadronization effects the jet tagging. The bulkgraviton \rightarrow WW and bulkgraviton \rightarrow HH are used for the W-jets and Higgs-jets respectively. First, we calcuate the efficiency of both jets in two models: PYTHIA and HERWIG. Then, for each model, we divide the ε_{HH} by ε_{WW} to get the efficiency ratio, referred as R. Finally, the systematic uncertainty is derived from the uncertainty of double ratio R_{HERWIG}/R_{PYTHIA} . There is p_T dependent uncertainty by fitting to the uncertainties of different mass point, which gives overall 13 to 19 % uncertainty[14].

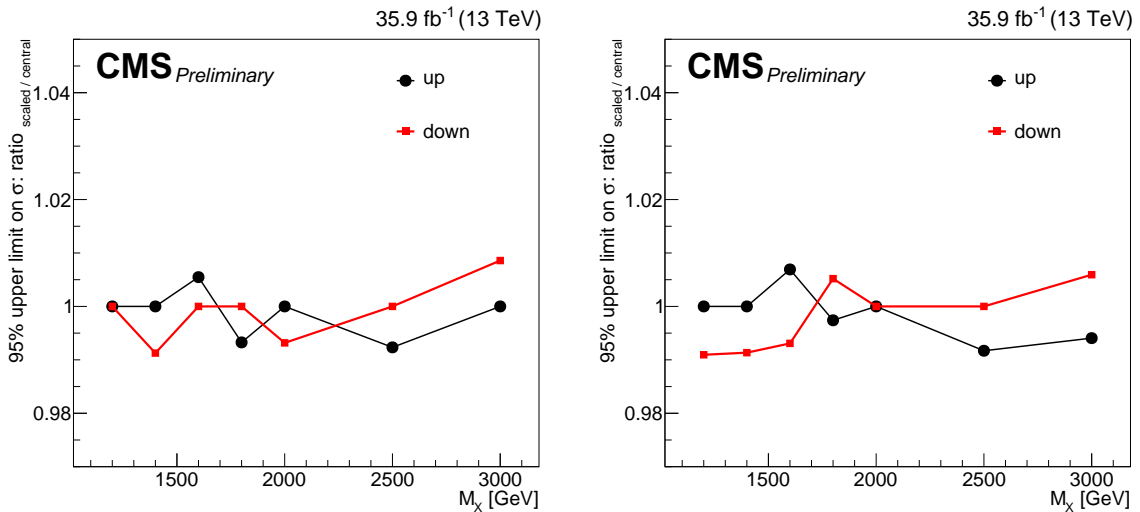


FIGURE 5.1: The pile-up uncertainty. The scale-up and scale-down to central ratio based on the change of the upper limit are shown in TT (left) and LL (right) category.

- Double-b tagger scale factor: The double-b tagger scale factor and its uncertainty is provided by BTV POG[50].
- τ_{21} scale factor: The uncertainty of τ_{21} scale factor is measured by JME POG on the samples of semi-leptonic $t\bar{t}$ which is a generous source of W boson. The uncertainty of scale factor in the region $\tau_{21} < 0.55$ is 14% per jet[48].
- Jet energy resolution: The procedure is to smear the energy resolution of AK8 jets of simulation as same as those of data[53].
- Parton distribution function, PDF: The parton distribution function is a probability density function of the energy of partons in a proton. The PDF is obtained only by experimental results. There are many sets of PDF trying to well describe them. In CMS, the NNPDF3.0 is used as default PDF set[54]. The uncertainty is derived from the ratio of RMS of the distribution of 100 efficiency by change the weight of different PDFs to the efficiency of the central PDF set.
- Factorization scale: the factorization is the energy determining separate the regimes of perturbative and non-perturbative of QCD. The uncertainty is

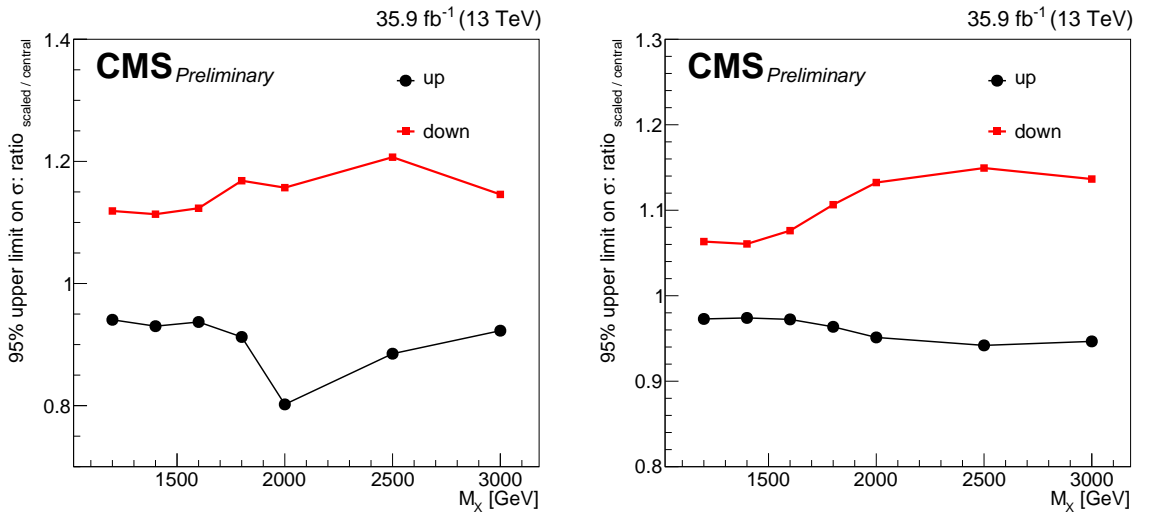


FIGURE 5.2: The double-b tagger uncertainty. The scale-up and scale-down to central ratio based on the change of the upper limit are shown in TT (left) and LL (right) category.

measured the changes of the efficiency by scaling the energy by two or by 0.5.

- Jet energy scale: The procedure is to weight the four momenta of AK8 jets of simulation as same as those of data[55]. The scale is to calibrate the energy response in ECAL of the jets using $gamma/Z + jets$ control samples because the energy of photon, of $Z \rightarrow e^+e^-$ and of $Z \rightarrow \mu^+\mu^-$ is measured accurately in ECAL.
- Trigger efficiency scale factor: the trigger efficiency scale factor is measured by the ratio of the efficiency of simulation to that of data. Since we veto the leptonic events, we use JetHt dataset instead of SingleMuon dataset to measure the efficiency of data. The uncertainty comes from propagating the statistic uncertainty added by $\frac{1 - efficiency_{PFJET260,QCD}}{efficiency_{pre-selection}}$. The pre-selection is listed:
 - Two leading AK8 jets have $p_T > 300$ GeV and $|\eta| < 2.4$.
 - $105 < \text{corrected PUPPI soft-drop mass} < 135$.
 - $\Delta\eta(\text{two leading AK8 jets}) < 1.3$.

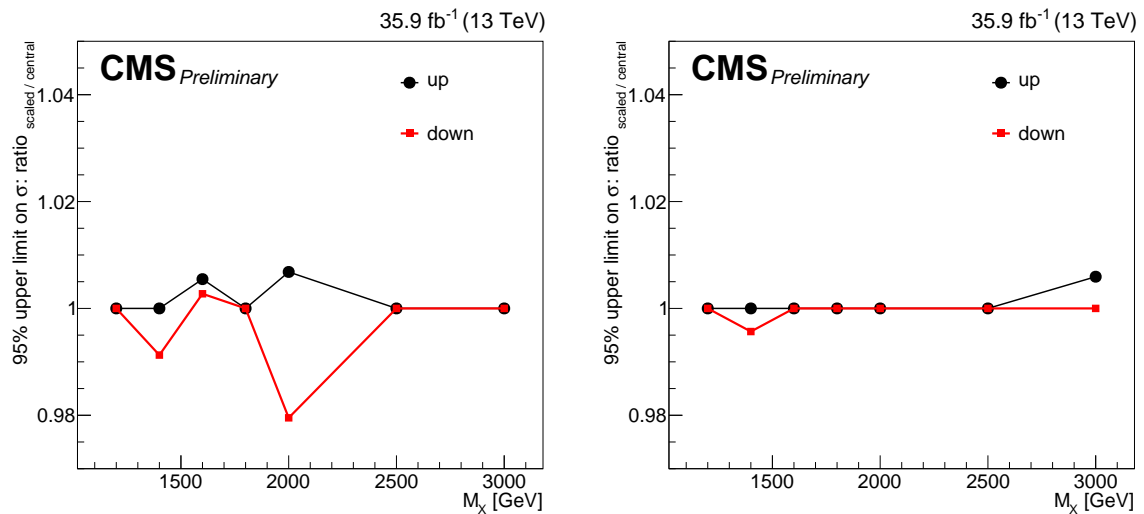


FIGURE 5.3: The jet energy resolution uncertainty. The scale-up and scale-down to central ratio based on the change of the upper limit are shown in TT (left) and LL (right) category.

The trigger efficiency scale factor effects less in the analysis because the M_{jj} of the signal is in the turn-on region where the scale factor is one.

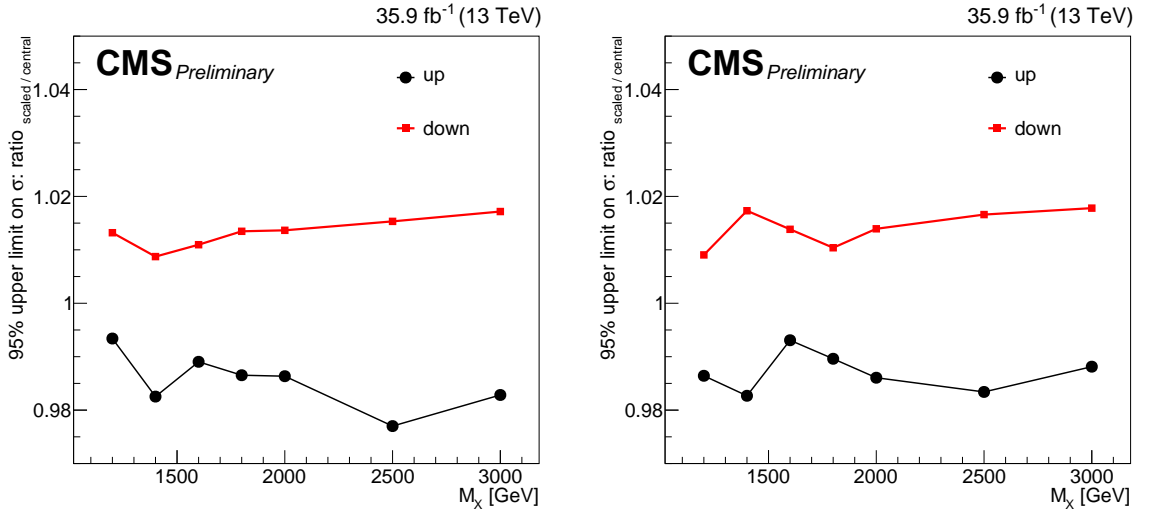


FIGURE 5.4: The jet energy scale uncertainty. The scale-up and scale-down to central ratio based on the change of the upper limit are shown in TT (left) and LL (right) category.

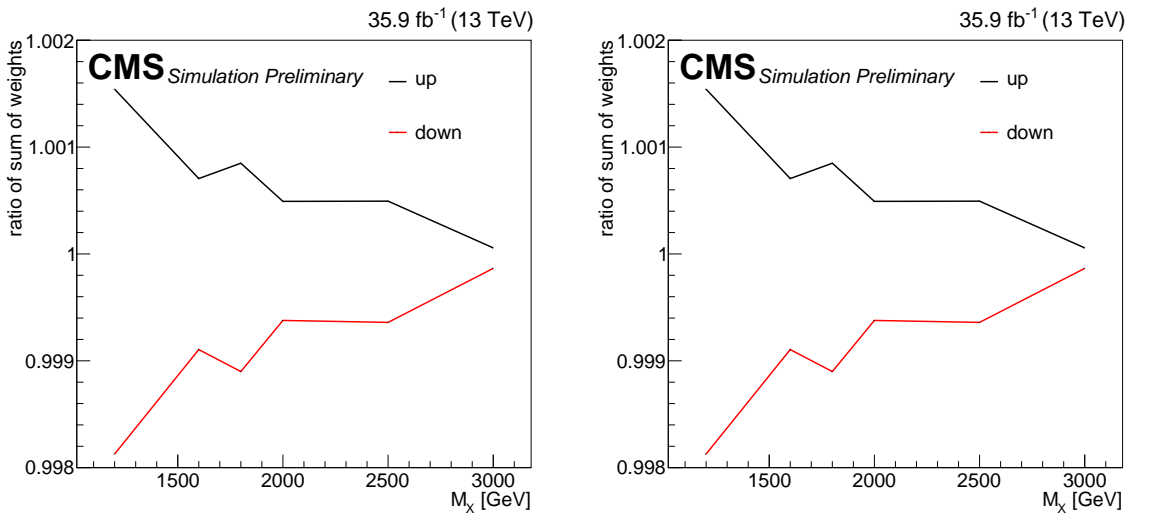


FIGURE 5.5: The Factorization uncertainty. The scale-up and scale-down to central ratio based on the change of the efficiecy are shown in TT (left) and LL (right) category.

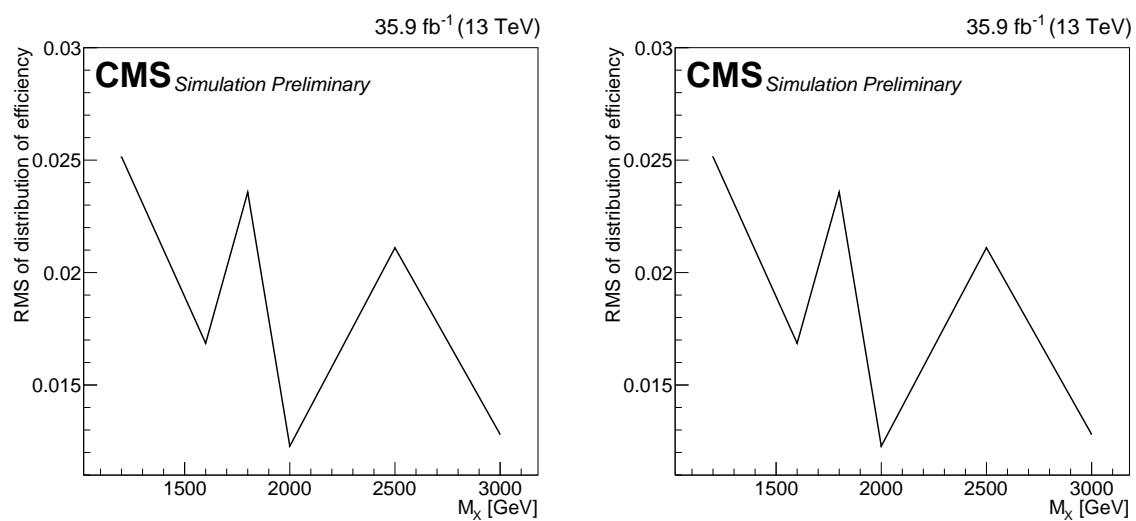


FIGURE 5.6: The jet energy scale uncertainty. The values of ratio RMS of efficiency from 100 p.d.f. sets to efficiency of central value are shown in TT (left) and LL (right) category.

5.2 Summary table

The summary of all systematic uncertainties is in table 5.1. It also concludes the variation form the uncertainted is considered.

| Uncertainty | value(TT) | value(LL) |
|--------------------------|----------------|----------------|
| Luminosity | 2.5% | 2.5% |
| Pile-up | 1% | 1% |
| Jet Energy Resoultion | 1% | 0.5% |
| Jet Energy Scale | 2% | 2% |
| Double-b tagger | 20% at most | 15% at most |
| Higgs tagging trigger | 13-19% | 13-19% |
| τ_{21} scale factor | less than 0.1% | less than 0.1% |
| PDF | 14% per jet | 14% per jet |
| scale | 2.5% | 2.5% |
| | 0.2% | 0.2% |

TABLE 5.1: List of systematic uncertainties and their values.

Chapter 6

Final Result

The final result based on the 95% CLs of upper limit on signal cross section \times branch ratio ($pp \rightarrow X \rightarrow HH \rightarrow b\bar{b}b\bar{b}$) is shown in the chapter.

6.1 Asymptotic CLs

The analysis uses CLs to find the upper limit of cross section[56, 57]. The CLs method tests whether the data is more consistent with a signal + background hypothesis or with a background-only hypothesis when the statistic of data is low. The CLs method starts with calculating likelihood ratio of the two hypotheses.

$$Q = \frac{\mathbf{L}(N_{data}, N_S + N_B)}{\mathbf{L}(N_{data}, N_B)}$$
$$\mathbf{L}(n, x) = \frac{e^{-x}}{n!} x^n \quad (6.1)$$

Then, the probability density function on $-2\ln(Q)$ of the two hypotheses are generated by toy-experiments using $N_S + N + B$ and $N + B$ as N_{data} in the equation separately. The CL_{s+b} represents the probability of results less consistent with a signal + background hypothesis, while the CL_b represents the probability of results less consistent with a background-only hypothesis.

$$CL_{s+b} = P_{s+b}(\ln Q \leq \ln Q_{obs}) = \int_{-\infty}^{\ln Q_{obs}} \frac{dP_{s+b}}{d\ln Q} d\ln Q \quad (6.2)$$
$$CL_b = P_b(\ln Q \leq \ln Q_{obs}) = \int_{-\infty}^{\ln Q_{obs}} \frac{dP_b}{d\ln Q} d\ln Q$$

The CLs defined as

$$CL_s = \frac{CL_{s+b}}{CL_b} \quad (6.3)$$

can be approximately seen as signal-only hypothesis. The 95% confidence level of CLs means that the probability to observe the data exceeding the signal + background hypothesis which is normalized to the probability to observe the data exceeding the background-only hypothesis is less than 5 %. The observed exclusion of 95% confidence level of CLs is calculated by integrating to a given lnQ_{obs} where $CLs < 0.05$. The expected exclusion limit is done in same procedure where lnQ_{obs} is replaced by lnQ_b in the equation. The Asymptotic CLs is obtained by CMS Higgs combination tool[58].

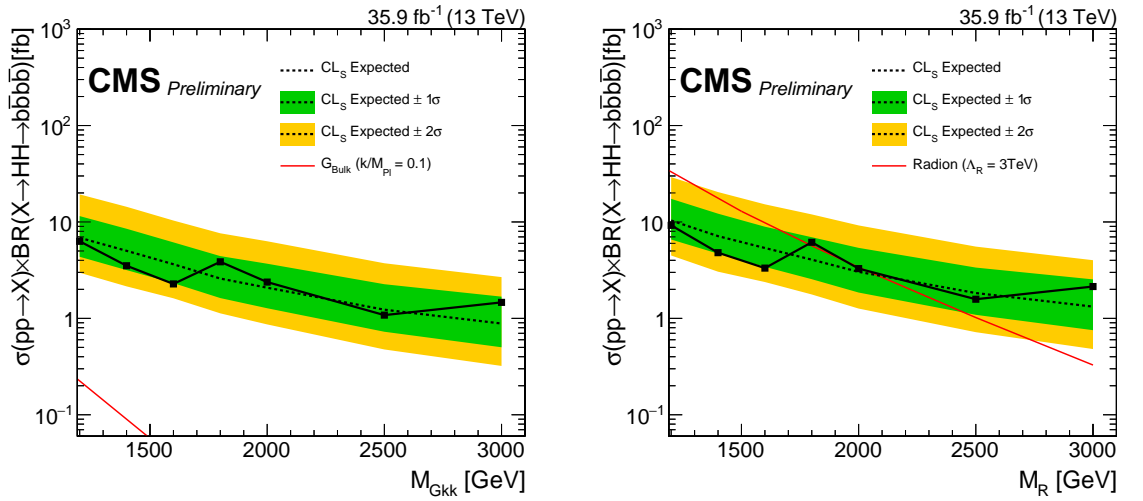


FIGURE 6.1: The 95% upper limit on signal cross section \times branch ratio ($pp \rightarrow X \rightarrow HH \rightarrow b\bar{b}b\bar{b}$) of bulk graviton (left) and radion (right).

| Mass Point (GeV) | Upper Limit (fb) | | | |
|------------------|--------------------|--------------------|---------------------------|---------------------------|
| | Radion Expected | Radion Observed | Bulk Graviton Expected | Bulk Graviton Observed |
| 1200 | 10.0 | 9.2 | 6.9 | 6.3 |
| 1400 | 7.1 | 4.8 | 5.0 | 3.5 |
| 1600 | 5.4 | 3.3 | 3.6 | 2.3 |
| 1800 | 4.1 | 6.2 | 2.6 | 3.9 |
| 2000 | 3.0 | 3.3 | 2.1 | 2.4 |
| 2500 | 1.8 | 1.6 | 1.2 | 1.1 |
| 3000 | 1.3 | 2.1 | 0.9 | 1.5 |

TABLE 6.1: The table of 95% upper limit on signal cross section \times branch ratio ($pp \rightarrow X \rightarrow HH \rightarrow b\bar{b}b\bar{b}$).

6.2 95% upper limit

The figure 6.1 shows the 95% upper limit on signal cross section \times branch ratio ($pp \rightarrow X \rightarrow HH \rightarrow b\bar{b}b\bar{b}$) of both signal. For bulk graviton, we didn't exclude any region, and the upper limit is below 10 fb with $k/M_{Pl} = 0.1$. On the other hand, we excluded the region of m_R below 1787 GeV and from considering $\Lambda_R = \text{TeV}$.

6.3 Conclusion

Searches for heavy resonances above 1.2 TeV decaying to a pair of Higgs bosons in the four b quark final state using 35.9fb^{-1} proton-proton collision data at center-of-mass energy 13 TeV collected with the CMS detector at the LHC are presented. The background is estimated by alphabet assisted bump hunt. The systematic uncertainties are mainly from double- b tagger scale factor, Higgs tagging, and τ_{21} scale factor. Bulk graviton and Radion are considered as signal. There is no excess from expected background in data. The 95 % confident level CLs of upper limit on cross section \times branch ration ($\text{pp} \rightarrow X \rightarrow \text{HH} \rightarrow b\bar{b}b\bar{b}$) of both signal are below 10 fb above 1.2 TeV. Bulk graviton is not excluded in the mass region from 1.2 TeV to 3 TeV, while radion is excluded from 1200 GeV to 1787 GeV and from 1964 GeV to 2078 GeV.

Bibliography

- [1] Matteo Cacciari and Gavin P. Salam. "Pileup subtraction using jet areas". In: *Phys. Lett. B* 659 (2008), p. 119. DOI: 10.1016/j.physletb.2007.09.077. arXiv: 0707.1378 [hep-ph].
- [2] Georges Aad et al. "Observation of a new particle in the search for the Standard Model Higgs boson with the ATLAS detector at the LHC". In: *Phys. Lett. B* 716 (2012), p. 1. DOI: 10.1016/j.physletb.2012.08.020. arXiv: 1207.7214 [hep-ex].
- [3] Lisa Randall and Raman Sundrum. "A large mass hierarchy from a small extra dimension". In: *Phys. Rev. Lett.* 83 (1999), p. 3370. DOI: 10.1103/PhysRevLett.83.3370. arXiv: hep-ph/9905221 [hep-ph].
- [4] Alexandra Oliveira. "Gravity particles from Warped Extra Dimensions, a review. Part I - KK Graviton". Submitted on arXiv. 2014.
- [5] H. Davoudiasl, J. L. Hewett, and T. G. Rizzo. "Phenomenology of the Randall-Sundrum Gauge Hierarchy Model". In: *Phys. Rev. Lett.* 84 (2000), p. 2080. DOI: 10.1103/PhysRevLett.84.2080. arXiv: hep-ph/9909255 [hep-ph].
- [6] Kaustubh Agashe et al. "Warped Gravitons at the LHC and Beyond". In: *Phys. Rev. D* 76 (2007), p. 036006. DOI: 10.1103/PhysRevD.76.036006. arXiv: hep-ph/0701186 [hep-ph].
- [7] A. Liam Fitzpatrick et al. "Searching for the Kaluza-Klein Graviton in Bulk RS Models". In: *JHEP* 09 (2007), p. 013. DOI: 10.1088/1126-6708/2007/09/013. arXiv: hep-ph/0701150 [hep-ph].
- [8] Walter D. Goldberger and Mark B. Wise. "Modulus stabilization with bulk fields". In: *Phys. Rev. Lett.* 83 (1999), p. 4922. DOI: 10.1103/PhysRevLett.83.4922. arXiv: hep-ph/9907447 [hep-ph].
- [9] Csaba Csaki et al. "Cosmology of brane models with radion stabilization". In: *Phys. Rev. D* 62 (2000), p. 045015. DOI: 10.1103/PhysRevD.62.045015. arXiv: hep-ph/9911406 [hep-ph].
- [10] Csaba Csaki, Michael L. Graesser, and Graham D. Kribs. "Radion dynamics and electroweak physics". In: *Phys. Rev. D* 63 (2001), p. 065002. DOI: 10.1103/PhysRevD.63.065002. arXiv: hep-th/0008151 [hep-th].

- [11] Gian F. Giudice, Riccardo Rattazzi, and James D. Wells. "Graviscalars from higher dimensional metrics and curvature Higgs mixing". In: *Nucl. Phys. B* 595 (2001), p. 250. DOI: 10.1016/S0550-3213(00)00686-6. arXiv: hep-ph/0002178 [hep-ph].
- [12] Nishita Desai, Ushoshi Maitra, and Biswarup Mukhopadhyaya. "An updated analysis of radion-higgs mixing in the light of LHC data". In: *JHEP* 10 (2013), p. 093. DOI: 10.1007/JHEP10(2013)093. arXiv: 1307.3765 [hep-ph].
- [13] Kaustubh Agashe, Oleg Antipin, et al. "Warped Extra Dimensional Benchmarks for Snowmass 2013". In: *Community Summer Study 2013: Snowmass on the Mississippi (CSS2013) Minneapolis, MN, USA, July 29-August 6, 2013*. 2013. arXiv: 1309.7847 [hep-ph]. URL: <http://cp3-origins.dk/research/units/ed-tools>.
- [14] Vieri Candelise, Ching-Wei Chen, Alice Cocoros, Leonardo Giannini, Maxime Gouzevitch, Raman Khurana, Michael Krohn, Gregorio de Leon III, Devdatta Majumder, Petar Maksimovic, Marc Osherson, Andrea Rizzi, Caterina Vernieri, Steve Wagner, Shin-Shan Eiko Yu. *Search for heavy resonances decaying to a pair of Higgs bosons in the four b quark final state in proton-proton collisions at $\sqrt{s} = 13$ TeV*. CMS Analysis Note 2016/300_v8. CERN, 2017. URL: http://cms.cern.ch/icMS/jsp/openfile.jsp?tp=draft\&files=AN2016_300_v8.pdf.
- [15] Stefano Catani et al. "Soft gluon resummation for Higgs boson production at hadron colliders". In: *JHEP* 07 (2003), p. 028. DOI: 10.1088/1126-6708/2003/07/028. arXiv: hep-ph/0306211 [hep-ph].
- [16] S Heinemeyer et al. "Handbook of LHC Higgs Cross Sections: 3. Higgs Properties". Submitted on arXiv. 2013.
- [17] Pavel M. Nadolsky et al. "Implications of CTEQ global analysis for collider observables". In: *Phys. Rev. D* 78 (2008), p. 013004. DOI: 10.1103/PhysRevD.78.013004. arXiv: 0802.0007 [hep-ph].
- [18] Johann Brehmer et al. "The Diboson Excess: Experimental Situation and Classification of Explanations; A Les Houches Pre-Proceeding". Submitted on arXiv. 2015.
- [19] Vardan Khachatryan et al. "Search for massive resonances in dijet systems containing jets tagged as W or Z boson decays in pp collisions at $\sqrt{s} = 8$ TeV". In: *JHEP* 08 (2014), p. 173. DOI: 10.1007/JHEP08(2014)173. arXiv: 1405.1994 [hep-ex].

- [20] Georges Aad et al. “Search for resonant diboson production in the $\ell\ell q\bar{q}$ final state in pp collisions at $\sqrt{s} = 8$ TeV with the ATLAS detector”. In: *Eur. Phys. J. C* 75 (2015), p. 69. DOI: 10.1140/epjc/s10052-015-3261-8. arXiv: 1409.6190 [hep-ex].
- [21] Georges Aad et al. “Search for production of WW/WZ resonances decaying to a lepton, neutrino and jets in pp collisions at $\sqrt{s} = 8$ TeV with the ATLAS detector”. In: *Eur. Phys. J. C* 75 (2015). [Erratum: 10.1140/epjc/s10052-015-3593-4], p. 209. DOI: 10.1140/epjc/s10052-015-3425-6. arXiv: 1503.04677 [hep-ex].
- [22] Georges Aad et al. “Search for high-mass diboson resonances with boson-tagged jets in proton-proton collisions at $\sqrt{s} = 8$ TeV with the ATLAS detector”. In: *JHEP* 12 (2015), p. 055. DOI: 10.1007/JHEP12(2015)055. arXiv: 1506.00962 [hep-ex].
- [23] Georges Aad et al. “Combination of searches for WW , WZ , and ZZ resonances in pp collisions at $\sqrt{s} = 8$ TeV with the ATLAS detector”. Submitted to *Phys. Lett. B*. 2015.
- [24] Vardan Khachatryan et al. “Search for massive resonances decaying into pairs of boosted bosons in semi-leptonic final states at $\sqrt{s} = 8$ TeV”. In: *JHEP* 08 (2014), p. 174. DOI: 10.1007/JHEP08(2014)174. arXiv: 1405.3447 [hep-ex].
- [25] Vardan Khachatryan et al. “Search for resonant pair production of Higgs bosons decaying to two bottom quark-antiquark pairs in proton-proton collisions at 8 TeV”. In: *Phys. Lett. B* 749 (2015), p. 560. DOI: 10.1016/j.physletb.2015.08.047. arXiv: 1503.04114 [hep-ex].
- [26] Georges Aad et al. “Search for Higgs boson pair production in the $b\bar{b}b\bar{b}$ final state from pp collisions at $\sqrt{s} = 8$ TeV with the ATLAS detector”. In: *Eur. Phys. J. C* 75 (2015), p. 412. DOI: 10.1140/epjc/s10052-015-3628-x. arXiv: 1506.00285 [hep-ex].
- [27] CMS Collaboration. “The CMS experiment at the CERN LHC”. In: *Journal of Instrumentation* 3.08 (2008), S08004. URL: <http://stacks.iop.org/1748-0221/3/i=08/a=S08004>.
- [28] Tai Sakuma. *3D SketchUp images of the CMS detector*. <https://cms-docdb.cern.ch/cgi-bin/DocDB/ShowDocument?docid=11514>.
- [29] *Superconducting Magnet*. URL: <http://cms.web.cern.ch/news/superconducting-magnet>.
- [30] L.Possi et al. *Pixel Detectors From Fundamentals to Applications*. Springer-Verlag Berlin Heidelberg, 2006. ISBN: 3-540-28332-3.

- [31] Johan Alwall et al. “*MadGraph 5: going beyond*”. In: *Journal of High Energy Physics* 2011.6 (2011), p. 128. ISSN: 1029-8479. DOI: 10.1007/JHEP06(2011)128. URL: [http://dx.doi.org/10.1007/JHEP06\(2011\)128](http://dx.doi.org/10.1007/JHEP06(2011)128).
- [32] A. Oliveira. *Bulk graviton NLO cross sections in WED at 13 TeV*. 2016. URL: https://github.com/CrossSectionsLHC/WED/blob/master/KKGraviton_Bulk/GF_NLO_13TeV_ktilda_0p1.txt.
- [33] A. Oliveira. *Bulk radion NLO cross sections in WED at 13 TeV*. 2016. URL: https://github.com/CrossSectionsLHC/WED/blob/master/Radion_Bulk/GF_NLO_13TeV_LR_3TeV_k1_35.txt.
- [34] A. Oliveira. *Bulk graviton to HH decay branching fractions in WED*. URL: https://github.com/CrossSectionsLHC/WED/blob/master/KKGraviton_Bulk/Decay_long.txt.
- [35] A. Oliveira. *Bulk radion to HH decay branching fractions in WED*. URL: https://github.com/CrossSectionsLHC/WED/blob/master/Radion_Bulk/Decay_long_k1_35_arxiv1110.6452.txt.
- [36] M. Aaboud et al. “Measurement of the Inelastic Proton-Proton Cross Section at $\sqrt{s} = 13$ TeV with the ATLAS Detector at the LHC”. In: *Phys. Rev. Lett.* 117.18 (2016), p. 182002. DOI: 10.1103/PhysRevLett.117.182002. arXiv: 1606.02625 [hep-ex].
- [37] *MET Filter Recommendations for Run II*. <https://twiki.cern.ch/twiki/bin/view/CMS/MissingETOptionalFiltersRun2>. 2017. URL: <https://twiki.cern.ch/twiki/bin/view/CMS/MissingETOptionalFiltersRun2>.
- [38] CMS Collaboration. *Commissioning of the Particle-Flow Event Reconstruction with the first LHC collisions recorded in the CMS detector*. CMS Physics Analysis Summary CMS-PAS-PFT-10-001. CERN, 2010. URL: <http://cdsweb.cern.ch/record/1247373>.
- [39] CMS Collaboration. *Particle-Flow Event Reconstruction in CMS and Performance for Jets, Taus, and*. CMS Physics Analysis Summary CMS-PAS-PFT-09-001. CERN, 2009. URL: <http://cdsweb.cern.ch/record/1194487>.
- [40] Matteo Cacciari, Gavin P. Salam, and Gregory Soyez. “The anti- k_t jet clustering algorithm”. In: *JHEP* 04 (2008), p. 063. DOI: 10.1088/1126-6708/2008/04/063. arXiv: 0802.1189 [hep-ph].
- [41] Daniele Bertolini et al. “Pileup Per Particle Identification”. In: *JHEP* 10 (2014), p. 059. DOI: 10.1007/JHEP10(2014)059. arXiv: 1407.6013 [hep-ph].

- [42] *Jet Identification Recommendations for 13 TeV data analysis*. https://twiki.cern.ch/twiki/bin/view/CMS/JetID#Recommendations_for_13_TeV_data. 2015. URL: https://twiki.cern.ch/twiki/bin/view/CMS/JetID#Recommendations_for_13_TeV_data.
- [43] Andrew J. Larkoski et al. “Soft Drop”. In: *JHEP* 05 (2014), p. 146. DOI: 10.1007/JHEP05(2014)146. arXiv: 1402.2657 [hep-ph].
- [44] CMS Collaboration. *Search for heavy resonances in the W/Z-tagged dijet mass spectrum at 13 TeV*. CMS Analysis Note CMS-AN-16-235. CERN, 2016.
- [45] Jesse Thaler and Ken Van Tilburg. “Identifying Boosted Objects with N-subjettiness”. In: *JHEP* 03 (2011), p. 015. DOI: 10.1007/JHEP03(2011)015. arXiv: 1011.2268 [hep-ph].
- [46] Jesse Thaler and Ken Van Tilburg. “Maximizing Boosted Top Identification by Minimizing N-subjettiness”. In: *JHEP* 02 (2012), p. 093. DOI: 10.1007/JHEP02(2012)093. arXiv: 1108.2701 [hep-ph].
- [47] Iain W. Stewart, Frank J. Tackmann, and Wouter J. Waalewijn. “N-Jettiness: An Inclusive Event Shape to Veto Jets”. In: *Phys. Rev. Lett.* 105 (2010), p. 092002. DOI: 10.1103/PhysRevLett.105.092002. arXiv: 1004.2489 [hep-ph].
- [48] CMS Collaboration. *W/Z-tagging of Jets: Working points and scale factors*. CMS TWiki r40. CERN, 2016. URL: https://twiki.cern.ch/twiki/bin/view/CMS/JetWtagging#Working_points_and_scale_factors.
- [49] CMS Collaboration. *Identification of double-b quark jets in boosted event topologies*. CMS Physics Analysis Summary CMS-PAS-BTV-15-002. CERN, 2016. URL: <https://cds.cern.ch/record/2195743>.
- [50] *Usage of b Tag Objects for 13 TeV Data with 25ns bunch spacing and 80xReReco reconstruction*. <https://twiki.cern.ch/twiki/bin/viewauth/CMS/BtagRecommendation80XReReco>. 2017. URL: <https://twiki.cern.ch/twiki/bin/viewauth/CMS/BtagRecommendation80XReReco>.
- [51] CMS Collaboration. *Search for heavy resonances decaying to a pair of Higgs bosons in four b quark final state in proton-proton collisions at sqrt(s)=13 TeV*. CMS Physics Analysis Summary CMS-PAS-B2G-16-008. CERN, 2016. URL: <https://cds.cern.ch/record/2202811>.
- [52] CMS Collaboration. *CMS Luminosity Measurement for the 2016 Data Taking Period*. CMS Physics Analysis Summary CMS-PAS-LUM-17-001. CERN, 2017. URL: Inpreparation.

- [53] CMS Collaboration. *Jet Energy Resolution*. CMS TWiki r56. CERN, 2017. URL: <https://twiki.cern.ch/twiki/bin/view/CMS/JetResolution>.
- [54] Richard D. Ball et al. “Parton distributions for the LHC Run II”. In: *JHEP* 04 (2015), p. 040. DOI: 10.1007/JHEP04(2015)040. arXiv: 1410.8849 [hep-ph].
- [55] Serguei Chatrchyan et al. “Determination of Jet Energy Calibration and Transverse Momentum Resolution in CMS”. In: *JINST* 6 (2011), P11002. DOI: 10.1088/1748-0221/6/11/P11002. arXiv: 1107.4277 [physics.ins-det].
- [56] A L Read. “Presentation of search results: the CL s technique”. In: *Journal of Physics G: Nuclear and Particle Physics* 28.10 (2002), p. 2693. URL: <http://stacks.iop.org/0954-3899/28/i=10/a=313>.
- [57] Nicolas Chanon. *Statistical Tools in Collider Experiments*. https://people.phys.ethz.ch/~pheno/Lectures2012_StatisticalTools/slides/Chanon5.pdf. 2012. URL: https://people.phys.ethz.ch/~pheno/Lectures2012_StatisticalTools/slides/Chanon5.pdf.
- [58] CMS Collaboration. *Documentation of the RooStats-based statistics tools for Higgs PAG*. <https://twiki.cern.ch/twiki/bin/view/CMS/SWGuideHiggsAnalysisCombinedLimit>.

Appendix A

Optimization of the Selection

In chapter three, the selection of the analysis are presented, and $\Delta\eta$, mass of AK8 jet, and working points of double-b tagger have been optimized. The procedure will be introduced in the chapter.

A.1 $\Delta\eta$

The selection of $\Delta\eta$ is mainly to reject the multi-jet events. The optimization is done through changing the value of $\Delta\eta$ selection and picking up the one whose Punzi significance, $\frac{\varepsilon_{signal}}{1+\sqrt{N_{bkg}}}$, is the highest, where ε_{signal} is the efficiency of the signal and N_{bkg} is the the number of events of background (MC multi-jet events). Through the difference of different is little, the value of 1.1 or 1.2 is favored in low mass region, while larger values are suited for higher mass region. However, the $\Delta\eta$ will change the trigger trun-on curve. Hence, we decided to use 1.3 for all mass region for both signal samples.

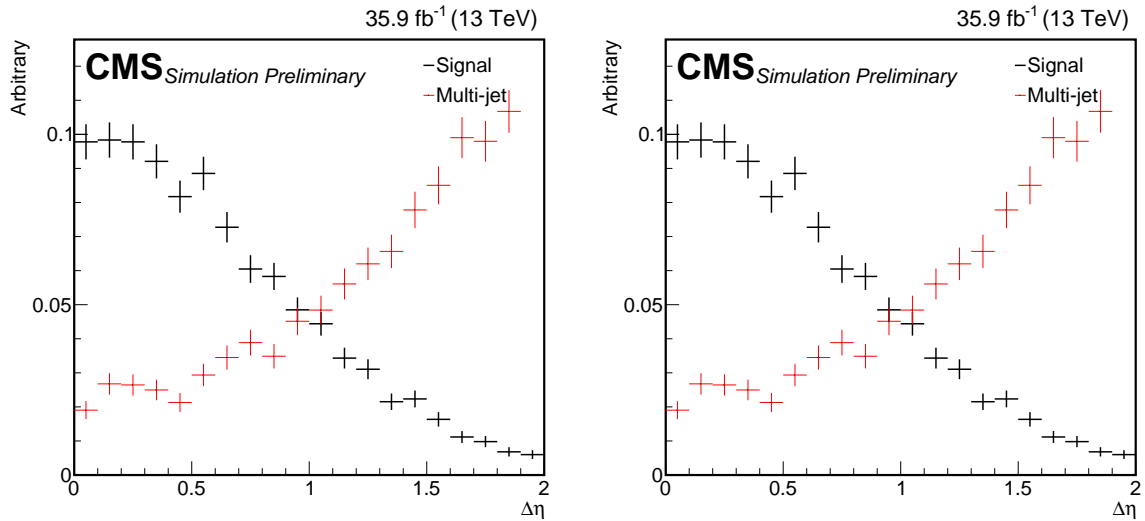


FIGURE A.1: The distribution of $\Delta\eta$ of 1.4 TeV bulk graviton and of multi-jet in TT (left) and LL (right) category.

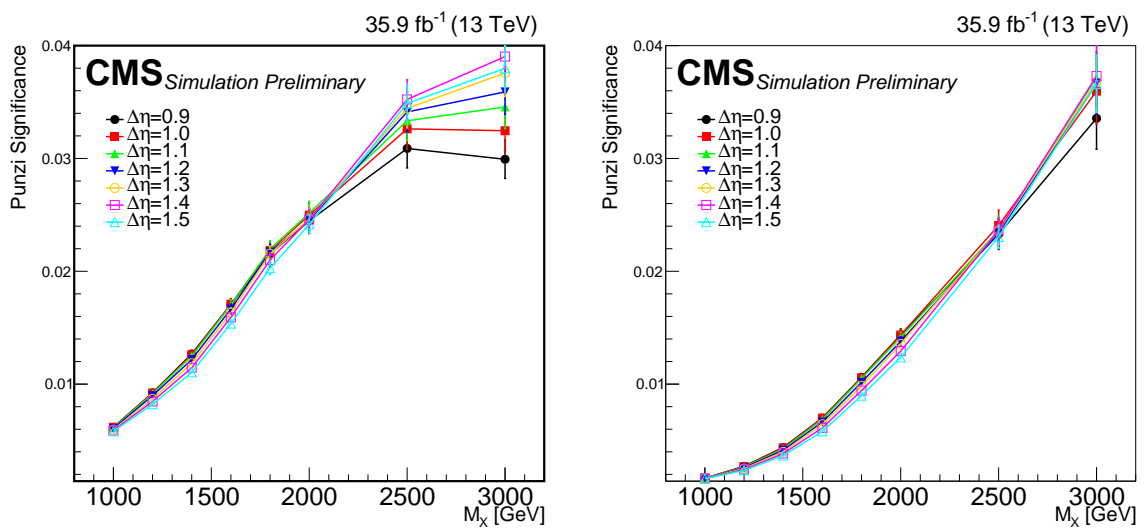


FIGURE A.2: The Punzi significance of different cut value of $\Delta\eta$ in TT (left) and LL (right) category of bulk graviton.

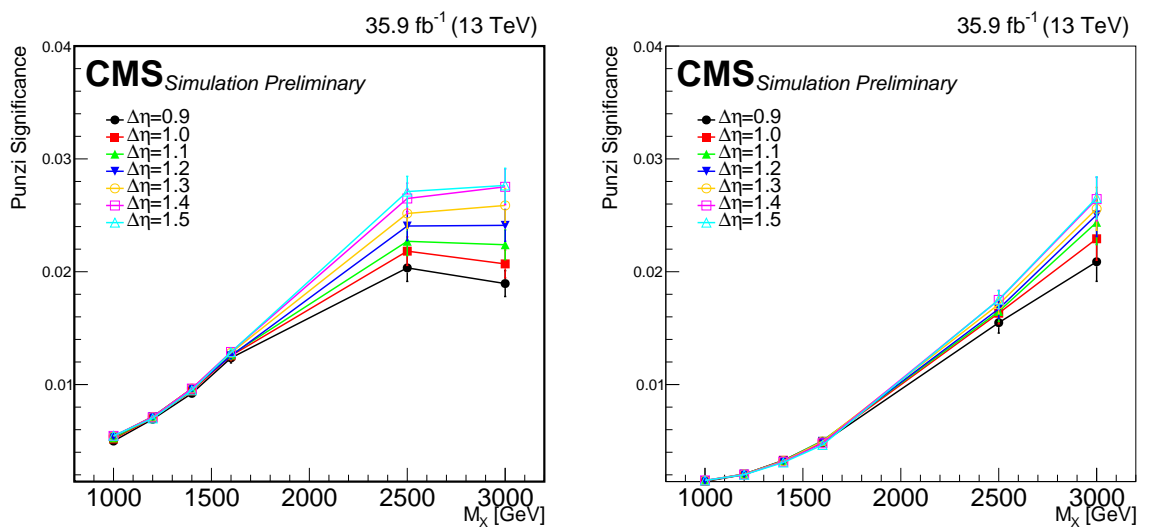


FIGURE A.3: The Punzi significance of different cut value of $\Delta\eta$ in TT (left) and LL (right) category of radion.

A.2 Double-b Tagger

There are two AK8 jets in an events of the analysis. Each AK8 jet corresponds to a working point of double-b tagger, either tight (>0.8), medium (>0.6), or loose (>0.3). The combinations are:

- TT: two passing tight.
- TM: one passing tight, the other passing medium.
- TL: one passing tight, the other passing loose.
- MM: two passing medium.
- ML: one passing medium, the other passing loose.
- LL: two passing loose.

The optimization is based on 95 % upper limit on $\sigma(pp \rightarrow X \rightarrow HH) \times Br(HH \rightarrow b\bar{b}b\bar{b})$ by bump hunt background estimataion. The TT region gives the best limit. Therefore, we further combine TT category with other categories to see if there is any improvement. Noted that the result is compared with 2015 analysis using another algorithm of b tagger, sub-jet b tagger, in three of four sub-jets in two AK8 jets passing selection and in four of them passing selection, which are referred as 3b and 4b respectively. We consider these combinations where each category is excluded from TT category:

- TM+TT
- TL+TT
- MM+TT
- ML+TT
- LL+TT

The TT combined with LL gives the best limit.

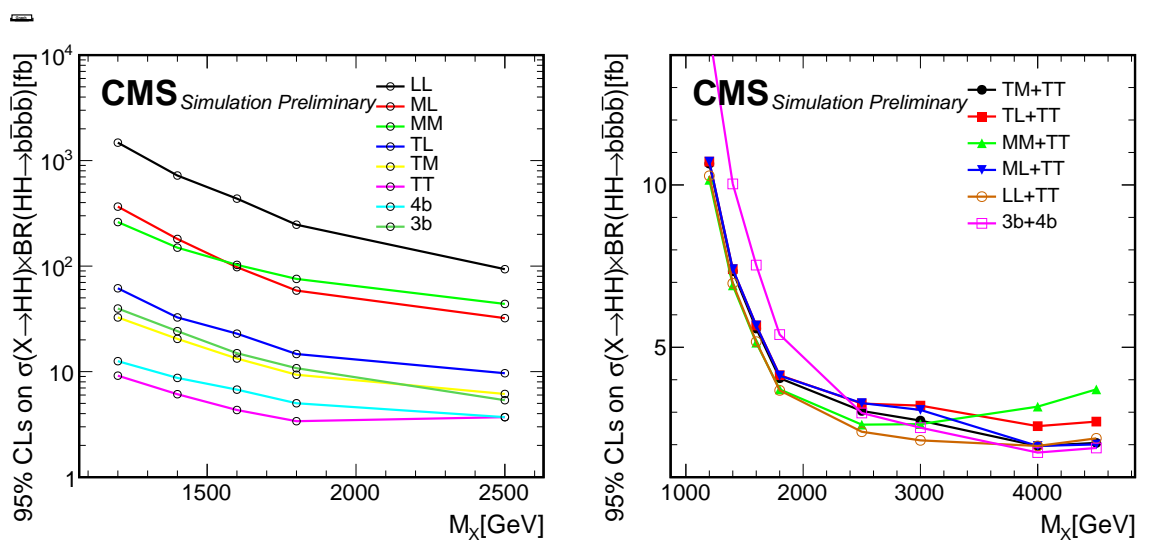


FIGURE A.4: The 95% upper limit on $\sigma(\text{pp} \rightarrow X \rightarrow \text{HH}) \times \text{Br}(\text{HH} \rightarrow b\bar{b}b\bar{b})$ with different double-b tagger category.

A.3 Mass of AK8 Jet

In order to tag the AK8 jet as Higgs jet, the selection around mass of Higgs boson is required, while the range should not cover the mass of Z boson and top quark. The width of the windows from 25 to 40 GeV is considered. All mass windows used are listed. Besides the PUPPI soft-drop mass with the W boson correction, the one with the Higgs dedicated correction is also targeted. The Higgs dedicated correction is done using similar procedure of the W boson correction. The samples are $X \rightarrow HH$ rather than $X \rightarrow WW$. In addition, the Higgs dedicated correction uses one-step correction, which corrects the mass of reconstruction-level to the mass of physical Higgs boson, while the W boson correction corrects first to generator-level then to the mass of physical Higgs boson. Both of them remove the dependence of the mass on jet p_T . The optimization is done based on 95 % upper limit on $\sigma(pp \rightarrow X \rightarrow HH) \times \text{Br}(HH \rightarrow b\bar{b}b\bar{b})$ by alphabet background estimation. The result shows that the mass with Higgs boson correction gives better limit of less than 10 %.

| Lower Range (GeV) | Width (GeV) | | | |
|-------------------|-------------|---------|----------------|----------------|
| | 25 | 30 | 35 | 40 |
| 100 | 100-125 | 100-130 | 100-135 | 100-140 |
| 105 | 105-130 | 105-135 | 105-140 | 105-145 |
| 110 | 110-135 | 110-140 | 110-145 | not considered |
| 115 | 115-140 | 115-145 | not considered | not considered |

TABLE A.1: The mass windows used for optimization.

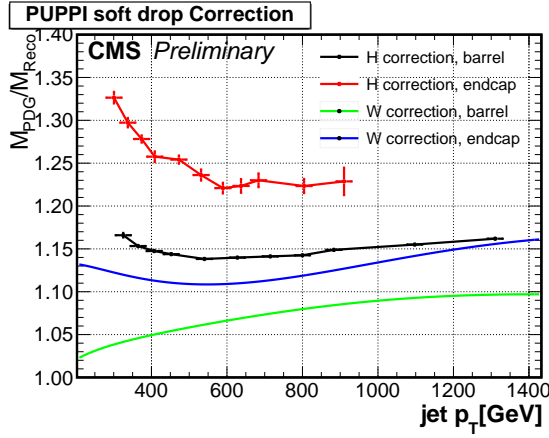


FIGURE A.5: The weights versus jet p_T of W boson and of Higgs boson correction.

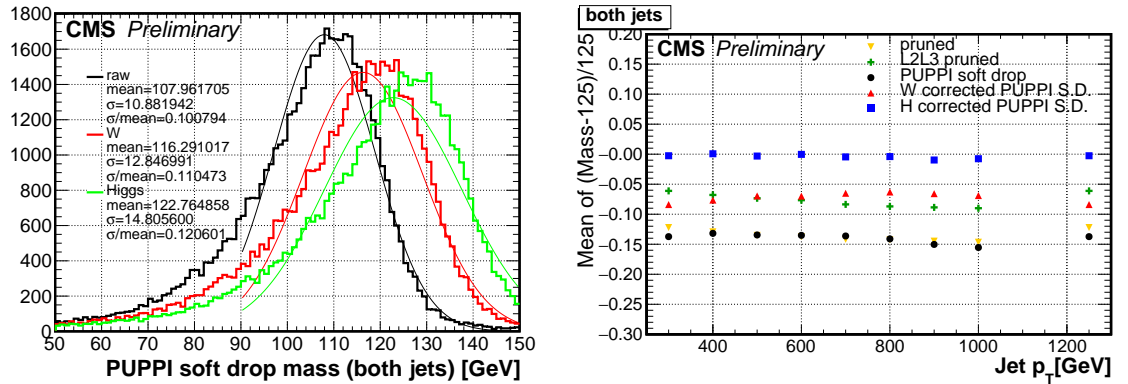


FIGURE A.6: The corrected PUPPI soft-drop mass (left) filled with leading and next leading AK8 jets and the mean of the Gaussian fit on the mass of versus the jet p_T (right). One point on the curve corresponds to one mass point of signal.

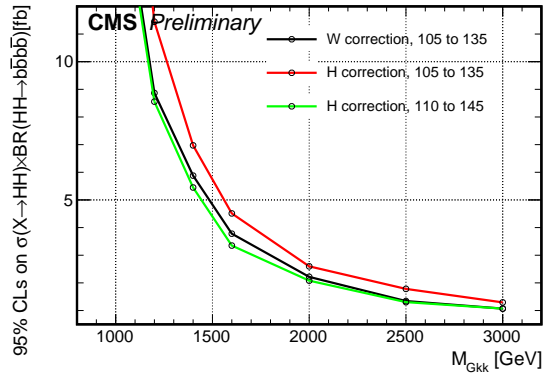


FIGURE A.7: The 95% upper limit on $\sigma(pp \rightarrow X \rightarrow HH) \times \text{Br}(HH \rightarrow b\bar{b}b\bar{b})$ with different mass windows of different mass correction.